Defence, Safety & Security
Oude Waalsdorperweg 63
2597 AK Den Haag
P.O. Box 96864
2509 JG The Hague
The Netherlands

www.tno.nl

T +31 88 866 10 00

TNO report

TNO 2022 R10073

Compensation of Atmospheric Effects on Radar (V1908)

Date	March 2023
Author(s)	Dr. Ir. Ph. van Dorp, Dr. Ir. J.J.M. de Wit
Classification report	Ongerubriceerd Releasable to the Public
Classified by	Ir. P. van de Maat
Classification date	25-01-2022
Title	Ongerubriceerd Releasable to the Public
Managementuittreksel	Ongerubriceerd Releasable to the Public
Report text	Ongerubriceerd Releasable to the Public
Appendices	Ongerubriceerd Releasable to the Public
No. of copies	1 cd
Number of pages	69 (incl. appendices, excl. distribution list)
Number of appendices	1
Project number	060.35407

The classification designation Ongerubriceerd is equivalent to Unclassified, Stg. Confidentieel is equivalent to Confidential and Stg. Geheim is equivalent to Secret.

Contents

Abbreviations

A2/AD	Anti-Access/Area Denial
ADS-B	Automatic Dependent Surveillance-Broadcast
BUFR	Binary Universal Form for Representation
COF	Cut-Off Frequency
DTED	Digital Terrain Elevation Data
ESM	Electronic Support Measures
GNSS	Global Navigation Satellite System
GPS	Global Positioning System
ITU	International Telecommunication Union
LEO	Low Earth Orbit
MALE	Medium Altitude, Long Endurance
MIMO	Multiple Input/Multiple Output
NWP	Numerical Weather Prediction
PE	Parabolic Equation
PPI	Plan Position Indicator
UAV	Unmanned Aerial Vehicle
UHF	Ultra High Frequency
VHF	Very High Frequency

1 Introduction

1.1 The Radar Programme

The goal of the Radar Programme V1908[1] is to develop and make available in a timely manner state-of-the-art radar knowledge and technology to be able to address future needs of the Netherlands armed forces concerning radar systems and sensor suites. As a guideline, the roadmap “Radar en Geïntegreerde Sensorsuites 2030” was used[2], which was outlined by the Platform Nederland Radarland in 2017. In this roadmap the operational needs, as identified by the Ministry of Defence, have been extended into required technical developments. The focus of the programme is mainly on the maritime domain, ensuring that (future) vessels of the Royal Netherlands Navy are able to operate worldwide under diverse circumstances. However, possible roads on how the developed knowledge can be applied in other domains (land, air and space) will be explored.
The introduction of comparable radar technology at other Operational Commands will lead to an increase in scale and lower life cycle costs. Also, the programme will allow TNO and Thales Nederland B.V., as partners in the Platform Nederland Radarland and other knowledge institutes and related industry to maintain or even enhance their good (international) position.

The programme focusses specifically on optimal radar suites able to counter future air threats in an adequate manner. For this, it is necessary to develop knowledge in the areas of novel integrated and reconfigurable radar and sensor suites, radar signal processing, and front-end technology. Further, research is required into possibilities to reduce life-cycle costs in relation to the reduction in manning on board of navy vessels. Within this programme, knowledge will be gained to ensure that Ministry of Defence radar systems can react optimally against contemporary, but also future, ever-increasing threats of advanced missiles and asymmetric threats.

For future missions of the Royal Netherlands Navy, the operational conditions become increasingly difficult to predict: threat characteristics change rapidly, weather extremes occur more frequently, varying theatres of operation become relevant and the lifecycle of platforms is extended. Consequently, the radar and sensor suite needs intrinsic adaptivity, flexibility and robustness to remain relevant throughout the lifespan of a platform. In addition, the coordinated operation of ships in a fleet is necessary to increase effectiveness against opponents with *anti-access/area denial* (A2/AD) capabilities. Within this frame, novel radar and sensor suite concepts are investigated that have the potential to offer the required performance, robustness and flexibility at the radar suite level, multiplatform level and task force level.

1.2 Compensation of Atmospheric Influences on Radar Measurements

Regarding future missions, navy platforms need to be prepared for operations in very diverse environments (tropics, Polar regions, open sea, littoral) and they need

[1] “Bestedingsovereenkomst Radarprogramma 2019-2022 (V1908),” TNO Defensie en Veiligheid, 2019.
[2] “Roadmap radar en geïntegreerde sensorsuites 2030,” Platform Nederland Radarland, 2017.

to handle suddenly occurring weather extremes and fluctuating atmospheric circumstances. The influence of the atmosphere and (extreme) weather conditions needs to be taken into account for accurate, reliable and consistent radar performance assessment and prediction.

The range and angle to a target, as measured by radar, depend on the current atmospheric conditions and the radar characteristics. Consequently, measurements of a specific target obtained by radars in different locations or by radars using different frequency bands, may not be mutually consistent due to varying propagation effects. The deviations in the absolute positioning of a target may be of the order of hundreds of metres [1], depending on the atmospheric conditions, radar parameters and measurement geometry. Furthermore, due to for instance *trapping* (refer to Section 2.3.3) a target may be detected by one radar system, but missed by another radar system in a different location. Such measurement inconsistencies complicate the fusion of observations made by radar systems in different locations or with different parameters (notably different operating frequency). Therefore, not in the least in view of future networked operations, it becomes very relevant to consider the effect of the current environmental conditions on radar wave propagation. (An extensive overview of the various atmospheric scattering mechanisms and propagation effects is provided in Chapter 2.)

By applying propagation models, the radar wave propagation can be predicted and with the aid of such models, radar measurements can be corrected for the effect of the atmosphere. However, the accuracy of the prediction and in turn the effectiveness of the correction depends highly on the accuracy of the atmospheric data and the frequency with which the meteorological parameters are acquired. The means to gather atmospheric data on board a navy platform on open sea are however limited. Therefore, within this project it was investigated whether information extracted from the radar measurements themselves can be used to compensate propagation effects, without the need for precise atmospheric data (Chapter 4). The feasibility of this approach was investigated for two different cases: when radar measurements in a single frequency band are available and when multiband radar measurements are available. The latter case is of interest for the integrated XS-Suite and the future integrated LSX-Suite.

Originally this study aimed at performing (multiband) radar measurements and analysing actual track data of, for instance, airliners flying over the North Sea. However, because of the COVID pandemic among others, there was no opportunity to perform measurements within the project duration. As a result, the approach shifted to using propagation models and historical atmospheric data for the analysis of propagation effects. In line with this shift, a brief inventory was made of available propagation models and it was decided to implement the *ray-optics* model, because this model provides the actual path length and path losses due to propagation, as function of frequency (Chapter 3). These models were used to analyse the aforementioned approach of using radar measurements themselves to compensate propagation effects.

Finally the conclusions and recommendations are given (Chapter 5).

2 Radar Wave Propagation

Radar waves propagating through the Earth's atmosphere are influenced by various propagation mechanisms. Depending on the actual atmospheric conditions, these mechanisms may result in propagation anomalies which may have a considerable effect on radar performance (either a positive or negative effect). A thorough review of atmospheric scattering mechanisms and tropospheric propagation effects can be found in [2] and [3]. The major propagation effects and their influence on radar performance, are briefly recapitulated in this chapter for quick reference. Note that Sections 2.2 through 2.4 are largely based on the information available in [2].

2.1 The atmosphere

The Earth's atmosphere is divided in four mayor layers: the troposphere, stratosphere, mesosphere and thermosphere (see Figure 2.1). For radar wave propagation in particular the lower layers, i.e., the troposphere and stratosphere ranging up to an altitude of about 50 km, are of importance. In addition the ionosphere has an impact on (low-frequency) radar wave propagation. As can be seen in Figure 2.1, the ionosphere is not a distinct atmospheric layer. The term ionosphere refers to several ionised layers embedded in the mesosphere and thermosphere. In the following subsections, the characteristics of the atmospheric layers and their effect on radar wave propagation are briefly discussed.

2.1.1 Ionosphere

The term ionosphere refers to several ionised layers in the Earth's atmosphere located between around 70 km and 1000 km altitude. The density of the ionised layers varies with the time of day. At night the lower layers (D and E) weaken or even vanish completely. After sunrise they strengthen again. The ionised gasses in the ionosphere can absorb, bend or reflect radar waves. This mechanism is exploited in low frequency (i.e., tens of MHz) over-the-horizon radar systems. Due to refraction or reflection by the ionised layers, the transmitted radar waves are directed back to the Earth's surface, covering a distance beyond the radar horizon. This effect is referred to as *skywave* propagation. The downward directed radar waves may reflect from the Earth's surface and then again be refracted or reflected by the ionised layers, covering even longer distances. The ionosphere also affects satellite communication and satellite navigation.

2.1.2 Stratosphere

The stratosphere is the layer roughly between 20 km and 50 km altitude. The temperature in this layer is assumed to be more or less constant and the water vapour content is low. The stratosphere is a relatively calm layer with negligible effect on radar wave propagation.

2.1.3 Troposphere

The troposphere is the lowest layer of the Earth's atmosphere extending from the Earth's surface to an altitude of around 20 km. The troposphere is a dynamic layer in which the temperature, pressure and water vapour content are variable, leading to variations of the refractive index. Due to the dynamic tropospheric conditions, most weather phenomena occur in this layer, e.g., the forming of turbulence, clouds

and precipitation. These phenomena have a major impact on radar wave propagation, as is explained in detail in Section 2.3.

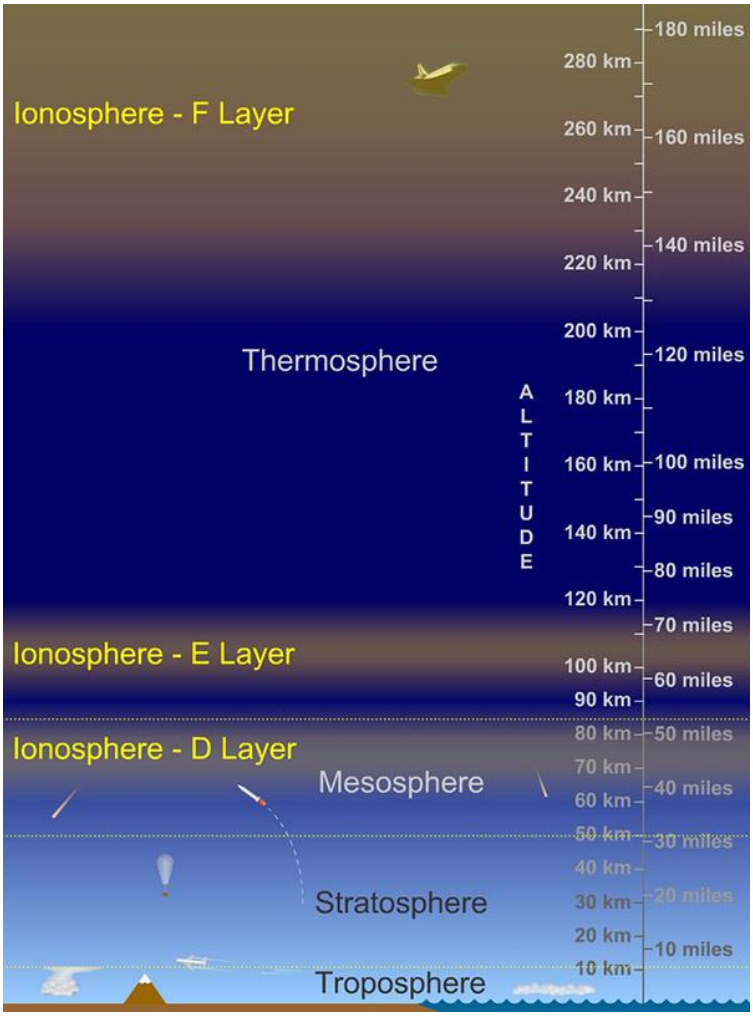

Figure 2.1 The layers of the Earth's atmosphere: troposphere, stratosphere mesosphere and thermosphere. By courtesy of [4].

2.2 Propagation Mechanisms

In this section, the major radar propagation mechanisms are briefly recapitulated.

2.2.1 Spherical Spreading

In free-space, the power radiated by an isotropic antenna spreads uniformly over an expanding spherical surface. Since the surface of a sphere is given as

$$A = 4\pi r^2, \tag{2.1}$$

where r is the sphere's radius, the power received at a certain point from the transmitting antenna is inversely proportional to the square of the distance between that point and the transmitting antenna.

2.2.2 Refraction

In an environment with constant refractive index, radar waves propagate along straight paths. When the refractive index varies along the wave's propagation path, either gradually or abrupt when the wave enters a different medium, the radar wave bends toward the region with the highest refractive index. This bending is governed by Snell's Law

$$n_1 \cos(\theta_1) = n_2 \cos(\theta_2), \tag{2.2}$$

in which n_1 and n_2 are the refractive indices of medium one and two and θ_1 and θ_2 are the incident angles of the incoming wave and refracted wave respectively, relative to the interface between the mediums.

Regarding radar waves, the refractive index is typically very close to one and impractical to use in propagation studies. Therefore, in propagation studies, the refractivity N

$$N = (n - 1) \cdot 10^6, \tag{2.3}$$

or the modified refractivity M

$$M \approx N + 0.157z, \tag{2.4}$$

is often used, where n is the refractive index and z is the altitude. The main advantage of the modified refractivity is that the Earth's curvature is taken into account such that in the Standard Atmosphere (see Section 2.3.1) the change of the modified refractivity $\mathrm{d}M$ divided by the change in altitude $\mathrm{d}z$ increases linearly. In trapping layers, on the other hand, $\mathrm{d}M$ divided by $\mathrm{d}z$ decreases, such that the modified refractivity is particularly suitable to visualise ducting effects in relation to altitude (see Section 2.3.3).

2.2.3 Specular Reflection

When striking a surface, i.e., an interface between media with different refractive indices, radar waves are reflected. When the surface is smooth, the angle between the interface's tangent plane and the reflected radar wave is equal to the angle between the incident radar wave and the interface's tangent plane. An interface can be considered 'smooth' if the interface's irregularities are much smaller than the radar wavelength. In general, when reflected, a radar wave is attenuated and its phase changes.

2.2.4 Diffuse Scattering

When striking a rough surface, only part of the radar wave is reflected in the specular direction. The remaining energy is scattered in all directions. The ratio between the specular reflected energy and the diffusely scattered energy, depends on the actual surface roughness (relative to the wavelength).

2.2.5 Beam Divergence

When a divergent beam of electromagnetic waves strikes a curved surface, the beam width increases upon reflection.

2.2.6 Multipath Interference

A transmitted radar wave may arrive at a certain point via multiple propagation paths. For instance, between a transmitter and receiver, a direct line-of-sight propagation path may exist and in addition an indirect path may exist via reflection upon a surface. Since the propagation paths to the receiver have different length, the two radar waves arriving at the receiver have different phase. At the receiver these two waves combine coherently, either in a destructive or constructive manner depending on the actual phase difference between the waves.

2.2.7 Diffraction

Diffraction refers to radar waves bending around the edges of an opaque object, propagating into what is the geometric *shadow zone* of the wave (i.e., the zone where there is no direct line-of-sight with the source of the radar wave). The energy of the wave propagating into the geometric shadow zone decays exponentially. Diffraction is a frequency-dependent propagation mechanism.

2.2.8 Attenuation

While propagating through the atmosphere, radar waves are attenuated by atmospheric gasses and weather, e.g., when propagating through rain, fog, snow or hail.

2.3 Tropospheric Propagation

In this section, the main radar propagation phenomena in the troposphere are briefly summarised.

2.3.1 Standard Propagation

As described in Section 2.1.3, the tropospheric conditions are dynamic and have a significant impact on radar wave propagation. To assess and compare different propagation conditions, ‘standard’ propagation conditions have been defined. These standard conditions are referred to as the Standard Atmosphere. In the Standard Atmosphere, the refractivity is assumed to decrease linearly with gradient

$$\frac{\mathrm{d}N}{\mathrm{d}z} = -39 \text{ N-units/km.} \tag{2.5}$$

This is an approximation of the exponential decrease of the refractivity N with increasing altitude, valid for altitudes below 1 km. This gradient causes radar waves to bend toward the Earth’s surface. As a result, the radar waves may travel beyond the geometrical (or optical) line-of-sight. In order to account for this effect, in propagation studies the effective earth radius, R_e, is commonly used. The effective earth radius is defined as

$$\frac{1}{R_e} = \frac{1}{R_E} + \frac{\mathrm{d}n}{\mathrm{d}z} \tag{2.6}$$

where R_E is the Earth's radius. Given the Standard Atmosphere, the effective earth radius is (4/3)R_E. Note that for standard propagation it is furthermore assumed that the Earth's surface is smooth, thus diffraction from terrain features is not taken into account.

If the actual atmospheric conditions differ from the Standard Atmosphere, the combined effect of the propagation mechanisms discussed in Section 2.2, may result in propagation that significantly differs from standard propagation. This is called *anomalous propagation*. Different types of anomalous propagation are discussed in the following sections.

2.3.2 *Anomalous Refraction*

Depending on the actual refractivity profile, three types of anomalous refraction can be distinguished as listed in Table 2.1. In Figure 2.2, the effect on radar wave propagation of anomalous refraction is schematically illustrated. Note that *anomalous* is not synonymous with irregular: ducting conditions may be persistent and exist for large percentages of the time [5].

Table 2.1 Refractive conditions and related refractivity gradients.

	d*N*/d*z* [N-units/km]	d*M*/d*z* [M-units/km]
subrefraction	0 < d*N*/d*z*	157 < d*M*/d*z*
normal*	-79 < d*N*/d*z* ≤ 0	79 < d*M*/d*z* ≤ 157
superrefraction	-157 < d*N*/d*z* ≤ -79	0 < d*M*/d*z* ≤ 79
trapping	d*N*/d*z* ≤ -157	d*M*/d*z* ≤ 0

* Note that this includes the conditions of the Standard Atmosphere.

Under certain atmospheric conditions, the refractivity may increase with increasing altitude. In these conditions radar waves are bent upward and away from the Earth's surface, rather than bent downward as in the Standard Atmosphere. This effect is referred to as *subrefraction* and may result in a significant reduction of the radar detection range. Generally speaking, subrefraction does not occur often.

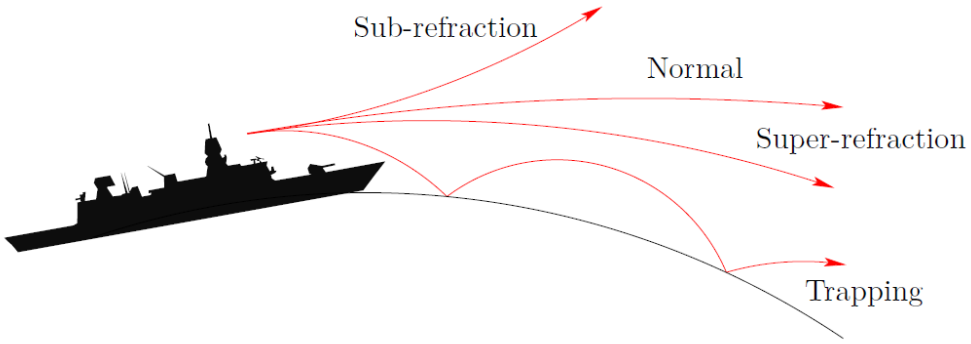

Figure 2.2 Schematic illustration of different refraction conditions. By courtesy of [2].

When the gradient of the refractivity is lower than in the Standard Atmosphere, radar waves may curve stronger toward the Earth's surface. If the curvature of the waves is still less than the curvature of the Earth, this effect is referred to as *superrefraction*. If the curvature of the radar waves is stronger than the curvature

of the Earth's surface, this effect is referred to as *trapping* (see Section 2.3.3). Both superrefraction and trapping may lead to extended radar detection ranges.

2.3.3 Trapping and Ducts

As explained in the previous section, in case of trapping conditions, a radar wave is strongly curved downward to the Earth's surface. Subsequently, it is reflected from the surface or refracted upward and propagates away from the surface. At some point the radar wave reenters the region with trapping conditions and it is refracted downward again. Thus the radar wave is effectively *trapped* in an atmospheric layer of certain width. Such a trapping layer is a so-called tropospheric *ducting layer*. Ducting has a major impact on radar performance. For instance, ducting may lead to significantly extended radar detection range. Note that radar waves are trapped in a ducting layer only for shallow angles of incidence. As a rule of thumb, the maximum angle of incidence, θ_{max}, for a radar wave to be trapped is

$$\theta_{max} = 0.081\sqrt{|\Delta N|}, \tag{2.7}$$

in which ΔN is the change in refractivity across the layer. In the maritime environment three different types of ducts are distinguished: the evaporation duct, the surface duct and the elevated duct. These different types of ducts are discussed in the following paragraphs.

Evaporation Duct

An evaporation duct is a persistent phenomenon, occurring nearly always and nearly everywhere over large bodies of water. An evaporation duct arises due to rapid decrease of humidity just above the water surface, a temperature inversion is not a prerequisite. The related vertical profile of the modified refractivity is shown in Figure 2.3. The altitude at which the minimum value of the modified refractivity occurs is the duct height. The evaporation duct height varies from 2 m at northern latitudes (at night) to 40 m in tropical areas (during summer days). The long-term global average evaporation duct height is 13 m. The ability of an evaporation duct to trap radar waves depends on the radar frequency; the lower the radar frequency is, the higher the duct needs to be to trap the radar waves. A rough indication of the lower frequency that will be trapped is given by the *cut-off frequency* (COF)

$$COF = 3.6 \cdot 10^{11} {z_e}^{-\frac{3}{2}}, \tag{2.8}$$

where z_e is the evaporation duct height. Regarding radar applications, the lower frequency that will be trapped in an evaporation duct is about 3 GHz. On open sea, where sea temperature and meteorological conditions can be assumed steady, an evaporation duct may extend up to hundreds of kilometres with almost constant duct height. In littoral regions, however, the duct height may vary considerably.

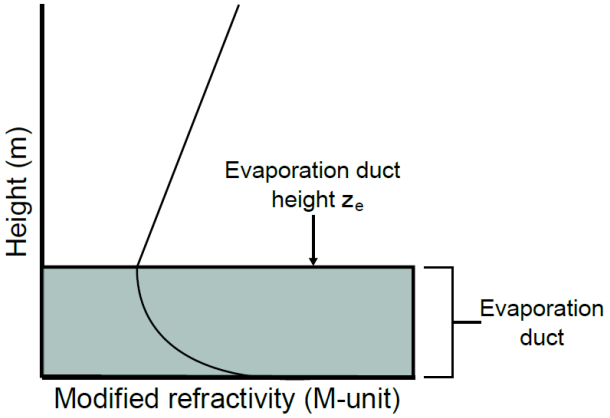

Figure 2.3 Modified refractivity profile of an evaporation duct. By courtesy of [3].

Surface Duct

Surface ducts arise due to a temperature inversion. They develop mainly over coastal waters such as the North Sea and over water bodies surrounded by warm, dry land such as the Mediterranean Sea and the Persian Gulf. In contrast to an evaporation duct, the effect of a surface based duct is essentially independent of frequency; frequencies as low as 20 to 100 MHz may be trapped in a surface duct. Surface ducts are less common than evaporation ducts, but their effect on radar propagation is much more dramatic. Surface ducts are responsible for most reports on extreme long over-the-horizon communication and radar detection ranges. This is because surface ducts can extend for hundreds of kilometres over open sea and exist for multiple days with duct heights of a few hundred metres.

If the trapping layer is located directly on the Earth's surface, the surface duct is called a *standard surface duct*. The vertical modified-refractivity profile of a standard surface duct is presented in Figure 2.4. The height of a standard surface duct is typically less than 200 m. The trapping layer within the surface duct may also be located several hundreds of meters above the Earth's surface, in this case the surface duct is called a *surface-based duct*. Refer to Figure 2.4 for a typical vertical modified-refractivity profile of a surface-based duct. The height of a surface-based duct can be up to 1000 m, but typically it is around 300 m. The main difference between standard surface ducts and surface-based ducts, is that surface-based ducts induce a so-called *skipping zone*. A skipping zone is the region occurring near the normal radar horizon, where the radar energy is low due to the ducting effect.

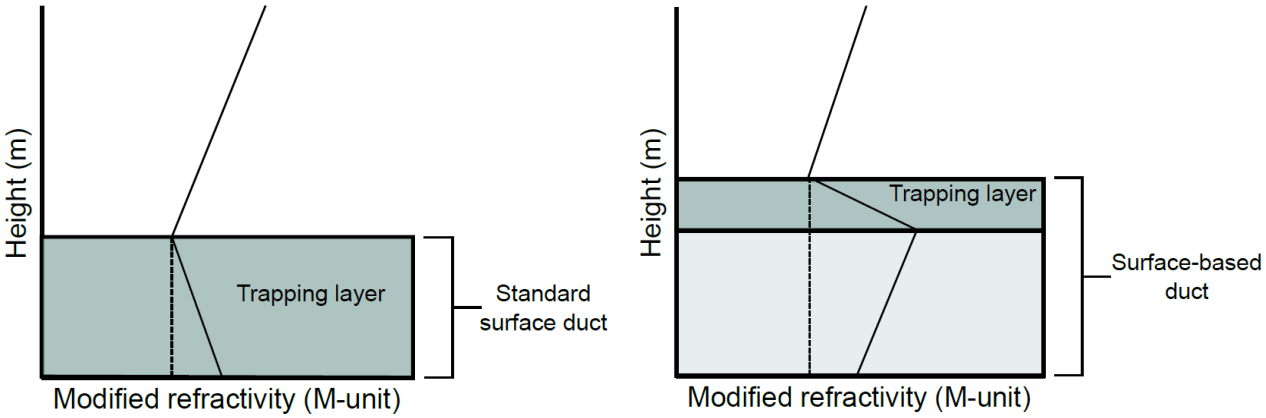

Figure 2.4 Modified refractivity profile of a standard surface duct (left) and a surface-based duct (right). By courtesy of [3].

Elevated Duct

If the duct and related trapping layer are completely elevated from the Earth's surface, the duct is called an elevated duct. A typical vertical profile of the modified refractivity of an elevated duct is shown in Figure 2.5. The thickness of an elevated duct may vary from zero to several hundred metres. Elevated ducts may arise at altitudes up to 6 km, but occur mostly below 3 km. They are more common in tropical areas. Similar to surface ducts, elevated ducts can affect radar propagation for frequencies as low as 100 MHz. As the other types of ducts, an elevated duct also gives rise to extended radar detection ranges, but only if the radar system and target are both at around the same altitude as the ducting layer. For a radar system located below (above) the elevated duct, the area above (below) the duct is actually shielded from the radar system creating a so-called *radar hole*.

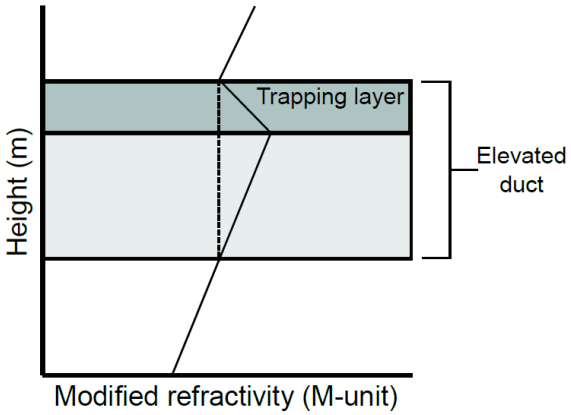

Figure 2.5 Modified refractivity profile of an elevated duct. By courtesy of [3].

2.3.4 *Lateral Inhomogeneity*

Typically the refractivity varies more in the vertical direction than in the horizontal direction. In particular over open sea, where the sea temperature and atmospheric conditions vary little, the atmosphere can be assumed homogenously stratified. In that case, the vertical refractivity profile may be steady for hundreds of kilometres and a single vertical refractivity profile can be applied to assess radar performance. The assumption of a homogenously stratified atmosphere is valid for around 86% of the time. In the littoral environment or in the vicinity of meteorological weather

fronts, however, the vertical refractivity profile may vary considerably as function of range, azimuth and time. Applying a single vertical refractivity profile for radar performance assessment in such variable conditions may result in significant performance prediction errors.

2.3.5 Terrain Effects

In the Standard Atmosphere propagation over a smooth surface is assumed. This is a reasonable assumption considering propagation over the open sea, but in littoral environments, the radar waves also propagate over terrain. Consequently, in littoral environments anomalous propagation due to irregular terrain features needs to be taken into account. The combined effect of diffuse surface scattering, multipath interference, diffraction around terrain features and refraction should be assessed. Note that due to diffuse surface scattering, a portion of the radar energy may be reflected back in the direction of radar leading to complex interference.

2.3.6 Troposcattering

Radar waves may travel beyond the radar horizon by reflection from refractive index inhomogeneities in the atmosphere located around the radar horizon. This phenomenon is referred to as troposcattering.

2.4 Radar Performance

The tropospheric conditions have a significant effect on radar wave propagation, as shown in the previous section. Depending on the actual atmospheric conditions, the propagation effects may have either a positive (e.g., increased detection range) or negative (e.g., shadow zones) effect on the radar performance and situation awareness, refer to Figure 2.6. In this section, the effect on radar performance and related situation awareness is briefly discussed.

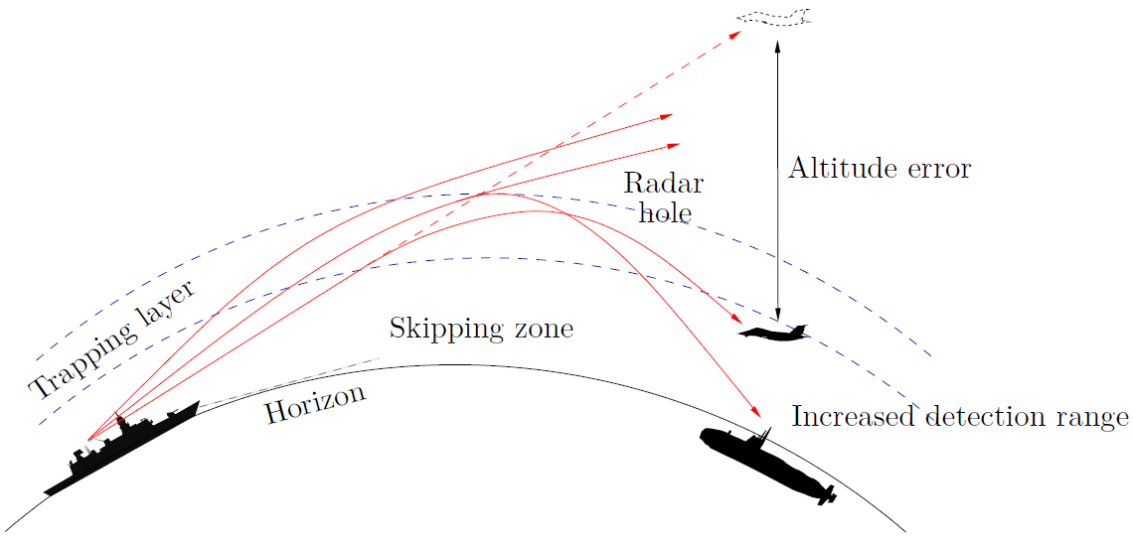

Figure 2.6 The effect of anomalous propagation on radar performance. By courtesy of [2].

2.4.1 Range Accuracy

Typically the range to a target is obtained by measuring the time between the transmission of a pulse and its reception and assuming the pulse travels with the Speed of Light. However, the Earth's atmosphere affects the velocity of propagation

of radar waves [6], [7]. In the atmosphere, the velocity of propagation is lower than the Speed of Light, depending on the temperature, pressure and in particular humidity. Since these parameters vary as function of altitude, also the velocity of propagation varies as function of altitude. If information on the current atmospheric conditions is available, the range between two points as measured by the radar, can be corrected for the variation of the velocity of propagation [7]

$$R_{true} \approx \left\{1 - \frac{H \cdot N_1 \cdot 10^{-6}}{h_2 - h_t}\left(1 - e^{\frac{-(h_2-h_1)}{H}}\right)\right\} R_{radar}, \tag{2.9}$$

in which R_{radar} is the range as measured by the radar, N_1 is the refractivity at the lower point, h_1 is the altitude of the lower point, h_2 is the altitude of the higher point and H is the refractivity exponential decay constant, defined as

$$H = \frac{h_2 - h_1}{\ln\left(\frac{N_1}{N_2}\right)}, \tag{2.10}$$

where N_2 is the refractivity at the higher point. Note that for this correction, the altitudes of the two points, h_1 and h_2, are an input and assumed known. The vertical refractivity profile is a required input as well.

Furthermore, due to refraction, radar waves travel along a curved path in the atmosphere. Consequently, the distance to a target as measured with a radar is longer than the direct geometric distance. This effect is however negligible compared to the variations of the velocity of radar wave propagation [7].

2.4.2 Elevation Accuracy

As stated in the previous section, radar waves travel along a curved path due to refraction on the atmosphere. Apart from an error in the measured range to a target, it also leads to an error in the measured elevation to that target, [8]-[12]. Since the measured elevation to a target is used to compute the target's height, an error in the measured elevation results in an error in the estimated target's height, as is visualised in Figure 2.6.

For small elevation angles, the total angle, τ, over which radar waves are bent due to refraction, can be approximated as [10]

$$\tau = \{(N_s \cdot 10^{-6})\cot(\theta)\}\left\{1.04 - \frac{1.07 \cdot 10^{-2}}{\theta} + \frac{1.28 \cdot 10^{-8}}{\theta^2} - \frac{1.23 \cdot 10^{-8}}{\theta^3}\right\}; \quad 2^{\circ} < \theta < 10^{\circ}, \tag{2.11}$$

where N_s is the refractivity at the surface and θ is the observed target's elevation angle. For larger elevation angles the total refraction can be approximated as [10]

$$\tau = (N_s \cdot 10^{-6})\cot(\theta); \quad 10 < \theta < 90^{\circ}. \tag{2.12}$$

With the aid of these approximate equations, the observed target's elevation can be corrected for the total refraction, if the refractivity at the surface is known.

2.4.3 Volume Coverage

Trapping of radar waves may lead to extended detection within the duct, but at the same time radar coverage outside the duct may be reduced due to radar holes and skipping zones. If the radar system is inside a duct, a target outside the duct may therefore go undetected, whereas it would have been detected in standard atmospheric conditions. Skipping zones may make it difficult to maintain steady, continuous tracks on surface targets or low-flying targets, since the detection probability reduces significantly inside the skipping zone. Note that whereas the radar energy 'leaking' into radar holes, skipping zones or shadow zones, is likely insufficient for target detection, it may be high enough to be intercepted by enemy electronic support measures (ESM) systems.

2.4.4 Detection Range

As a consequence of anomalous propagation, the radar detection range may increase significantly or decrease. Radar waves trapped in a duct may travel well beyond the radar horizon. This increases the detection range significantly. At the same time second-time-around or even third-time-around echoes are likely to occur. Note that multiple time around echoes from the (sea) surface or precipitation result in increased clutter levels. Furthermore, enemy electronic warfare will be effective over longer ranges (e.g., longer enemy ESM intercept range).

2.4.5 Target Radar Cross Section

Due to turbulence in the atmosphere, the observed backscatter of a target may vary [1]. This effect is referred to as *scintillation*. Scintillation is often observed during Very High Frequency (VHF) and Ultra High Frequency (UHF) propagation through the ionosphere.

3 Propagation Models

In this chapter some propagation models are discussed. For the current study, it is mandatory that the propagation models are frequency dependent, such that difference in propagation for X-band, S-band and L-band can be assessed. Since in particular the observed angle to a target is affected by propagation effects, the propagation models should furthermore provide the complex propagation factor to determine the observed angle-of-arrival (as explained in Section 3.2.2). Note that the ray-optics method described in Section 3.4, has been implemented and validated within the framework of this project, as a means to also assess variations of the path length and path losses due to propagation. This section starts with an introduction to propagation modelling.

3.1 Introduction

Barrios describes the APM CSCI propagation model [49]. The APM model is very similar to the TERPEM model and is used here to introduce the different propagation calculation techniques. The TERPEM model is described later. APM is a range-dependent true hybrid model that uses complimentary of Ray Optics (RO) and Parabolic Equation (PE) techniques to calculate propagation loss both in range and altitude. The atmospheric volume is divided into regions that lend themselves to the application of the various propagation loss calculation methods. The figure below illustrates these regions.

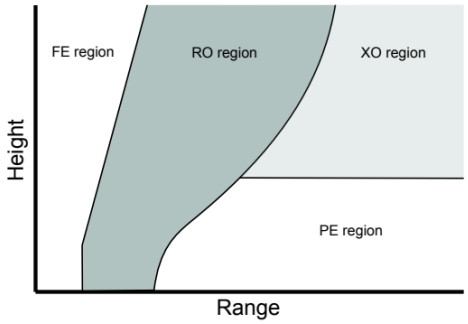

Figure 3.1 APM calculation regions [49].

For antenna elevation angles above 5 degrees or for ranges less than approximately 2.5 kilometres (km), a flat-earth (FE) ray-optics model could be used. In this region, only receiver height is corrected for average refraction and earth curvature.

Within the RO region (as defined by a limiting ray), propagation loss is calculated from the mutual interference between the direct-path and surface-reflected ray components using the refractivity profile at zero range. Full account is given to focusing or de-focusing along direct and reflected ray paths and to the integrated optical path length difference between the two ray paths, to give precise phase difference, and, hence, accurate coherent sums for the computation of propagation loss.

For the low-altitude region beyond the RO region, a PE approximation to the Helmholtz full wave equation is employed. The PE model allows for range-dependent refractivity profiles and variable terrain along the propagation path and uses a split-step Fourier method for the solution of the PE. The PE model in the minimum region required to contain all terrain and trapping layer heights.

For the area beyond the RO region but above the PE region, an extended optics region (XO) is defined. Within the XO region, ray-optics methods that are initialized by the PE solution from below, are used.

The propagation models are frequency dependent. Frequency agility and frequency diversity [47] [48] are the ability of a radar system to quickly shift its operating frequency in one band to account for atmospheric effects, jamming, mutual interference with friendly sources, or to make it more difficult to locate the radar broadcaster through radio direction finding. A change in the frequency will change the location of the nulls and lobes so that operating with multiple frequencies the nulls in elevation can be filled in. The process of selecting the frequencies in one band to mitigate multipath minima is call elevation null filling [48]. Elevation null filling selects the frequencies in a way the entire elevation range is filled and multipath effects are mitigated.

3.2 CARPET

CARPET[3] is a software tool for radar performance assessment developed by TNO [14]. The CARPET tool incorporates two different atmospheric propagation models: EREPS and TERPEM.

3.2.1 EREPS

A first order propagation model is EREPS [15], based on empirical models for radar wave propagation. EREPS has been developed to assist an engineer in assessing electromagnetic propagation effects of the lower atmosphere on radar, electronic warfare and communication systems. The EREPS models account for effects of optical interference, diffraction, tropospheric scatter, refraction, evaporation and surface-based ducting and water-vapor absorption under horizontally homogeneous atmospheric conditions. The EREPS propagation model is available in CARPET, The Mathworks Matlab and Python.

3.2.2 TERPEM

CARPET relies on TERPEM [16] for providing a quantitative numerical model for computing the effects of ducting and refraction in the atmosphere. TERPEM is based on fundamental models of electromagnetic propagation. It utilises computational methods based on the Parabolic Equation (PE) for modelling radar wave propagation taking into account the vertical refractivity profile as well as terrain effects. TERPEM calculates the path loss without phase information.
The absolute voltage propagation factor is derived from the path loss. The vertical refractivity profile and the terrain parameters can be set as a function of range.
A special version of TERPEM is available, which computes the complex propagation factor [17]. With the aid of this complex factor, the angle-of-arrival of received signals can be calculated [18], [19].

[3] Computer-Aided Radar Performance Evaluation Tool.

Within the current study, TERPEM has been used in two ways to calculate the elevation angle; with the voltage propagation factor and with fan beam pattern. These two methods are discussed in the following paragraphs.

Voltage Propagation Factor Elevation Estimation
The elevation angle is estimated with two antenna positions with vertical distance d with the monopulse radar principle. The calculation can be performed more accurately when more antennas are used. In this study, the monopulse radar approach is sufficient. The elevation angle θ is calculated based on the phase difference $\Delta\phi$ between the two antennas by

$$\theta = \arcsin\left(\frac{\lambda\,\Delta\phi}{2\pi\,d}\right). \tag{3.1}$$

In this equation λ is the wavelength. Two calculations of TERPEM at height h_1 and height h_2 give the two voltage propagation factors. The phase difference between these two factors is a measure of the elevation angle. The elevation angle is unambiguous if the height difference (i.e., the interelement spacing) is less than half the wavelength.

The voltage propagation factor is however not a standard output parameter of TERPEM. TERPEM solves the differential equations with a split-step Fourier algorithm. The output of this split-step Fourier algorithm gives the differential equation solution on the grid coordinates $vpf^*_{k_r,k_h}$ where k_r is the range index and k_h is the height index. This voltage propagation factor is complex and the delay of the transmitter to the grid point is not taken into account. The voltage propagation factor returned by TERPEM with this additional delay is

$$vpf_{k_r,k_h} = e^{i\frac{2\pi r_{k_r,k_h}}{\lambda}}\, vpf^*_{k_r,k_h}. \tag{3.2}$$

In this equation, r_{k_r,k_h} is the slant range between the transmitter and the object. PETOOL's source code gives a similar correction factor using the ground range instead of the slant range. This must be the slant range, otherwise no height differences are included in the phase correction factor. (The PETOOL software package is discussed in Section 3.3.)

Fan Beam Pattern Elevation Estimation
This method is based on the use of stacked fan beams to determine target elevation. It is assumed that eleven fan beams are stacked in elevation. The beamwidth of each fan beam is θ_e in elevation. The angular spacing in elevation, between the individual fan beams is equal to the beamwidth. The elevation to a target is now estimated by quadratic interpolation between the target responses received in three adjacent fan beams, where the centre beam has the highest target response. Some examples of this method are shown in Figure 3.2 and Figure 3.3. In this example the number of fan beams is eleven and the elevation beamwidth of each beam is 1°. As can be seen, in the lower fan beams, the multipath effects are significant and the estimation of a target's elevation will fluctuate strongly with the target's position. In the beams directed to higher elevation angles, the multipath effects diminish.

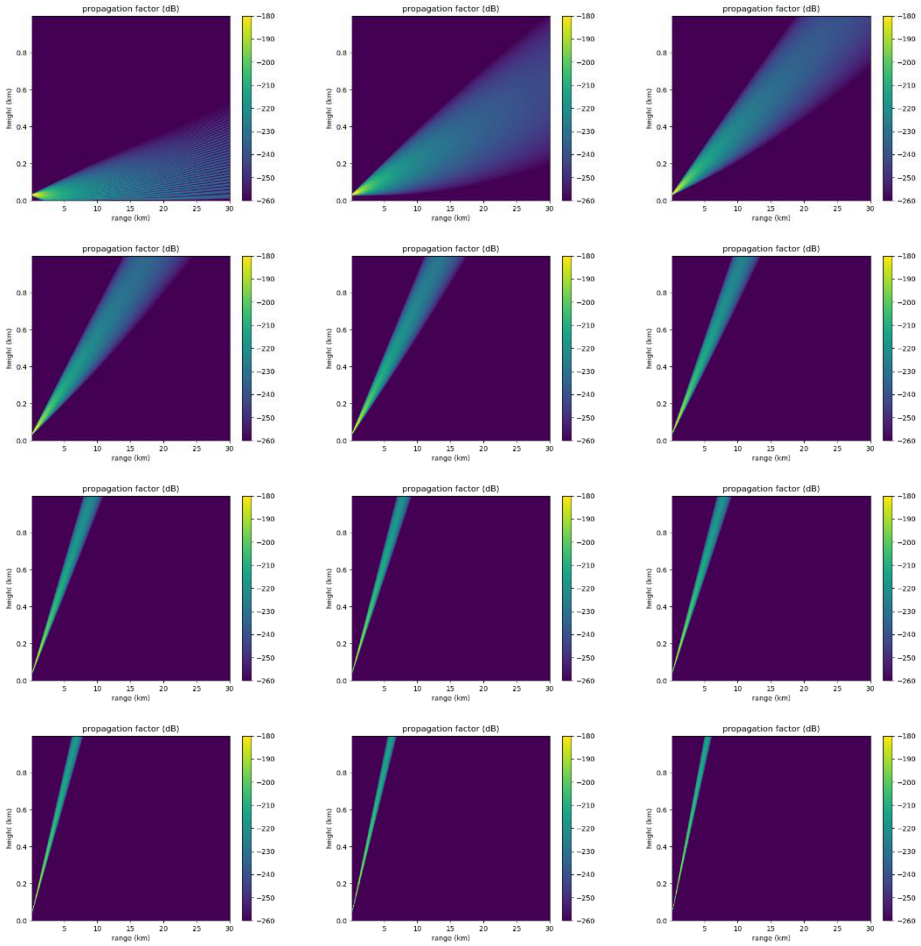

Figure 3.2 Example of the propagation factors for a X-band radar fan beam pattern with eleven beams stacked in elevation. The beam spacing is 1°. All eleven beams from 0° to 10 tilt angle are depicted. The propagation factor is based on the loss factor.

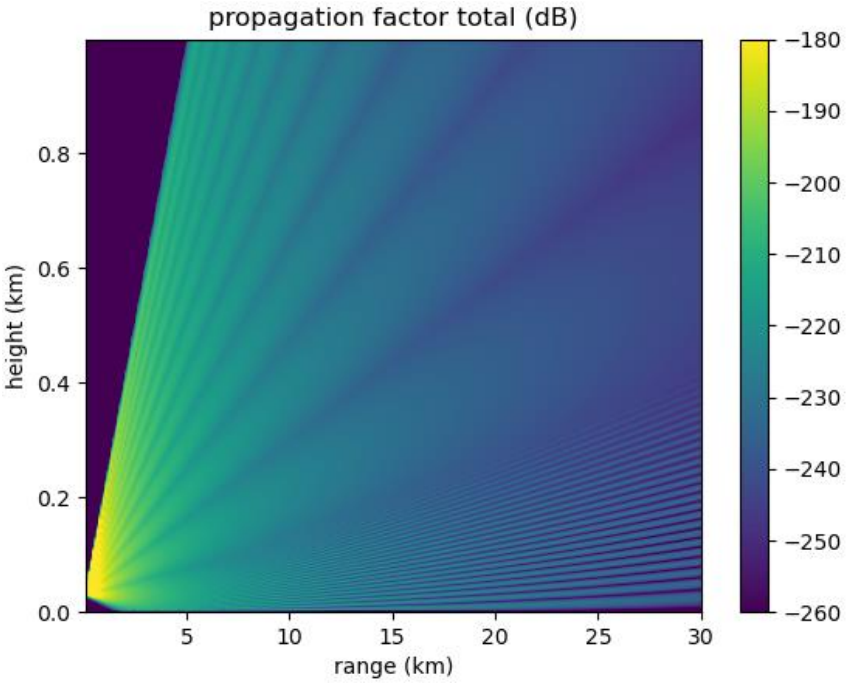

Figure 3.3 Example of the combined propagation factors for a X-band fan beam pattern with eleven beams stacked in elevation. The beam spacing is 1°. The propagation factor is based on the loss factor.

3.3 PETOOL

The PETOOL software tool, [20], [21], visualises radar wave propagation over variable terrain through a homogeneous or inhomogeneous atmosphere. It exploits a recursive forward-backward algorithm to incorporate both forward and backward waves into the solution in the presence of variable terrain. A drawback of PETOOL is that the individual rays are not provided, the results are available on the grid points only. Ray parameters are the path length in the medium, transmit angles and receive angles. PETOOL is not capable of estimating the spread in delay times (due to multiple propagation paths with different lengths) and the angle-of-arrival. PETOOL has been validated with the aid of other software packages, such as AREPS [22]. PETOOL's code has been discussed in literature [23]. This discussion is very useful for understanding the entire code, the approaches that have been taken and potential improvements that can be made.

PETOOL is a free open-source program with a graphical user interface developed in The Mathworks Matlab. An impression of the main user interface of PETOOL can be found in Figure 3.4 and an impression of the interface to define the vertical refractivity profiles is shown in Figure 3.5. All code is available and can be expanded depending on one's specific research needs.

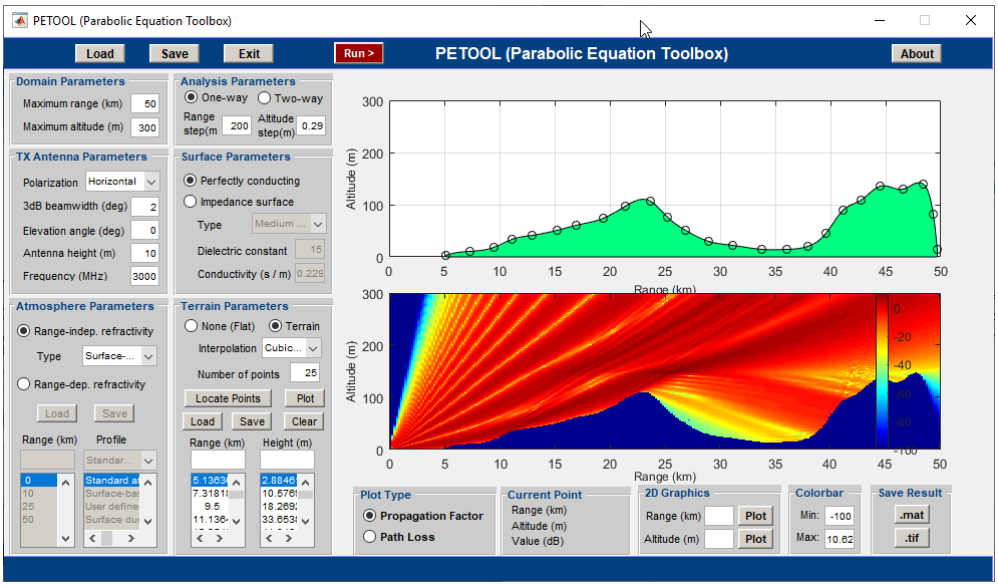

Figure 3.4 The PETOOL main user interface.

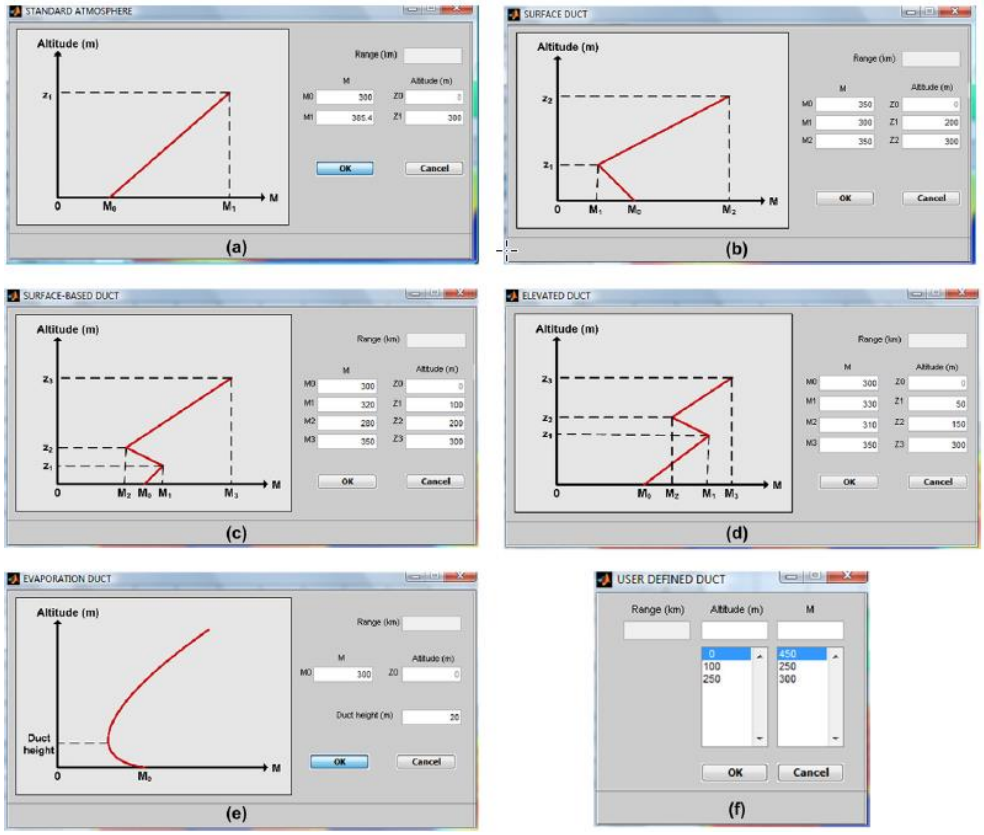

Figure 3.5 The PETOOL user interface to define the vertical refractivity profile, including the standard atmosphere (a), a surface duct (b), a surface-based duct (c), an elevated duct (d), an evaporation duct (e) and user-defined ducts (f).

Version 2.0 of PETOOL incorporates four new features:

1 Several evaporation duct models have been developed.
2 Real atmospheric data have been included: Binary Universal Form for Representation (BUFR data developed by the World Meteorological Organization).
3 Real terrain data have been incorporated: Digital Terrain Elevation Data (DTED) developed by the National Imagery and Mapping Agency.
4 Additions have been developed to generate a 3D coverage map of propagation factor/loss on real terrain data.

With the aid of these new features, horizontal coverage diagrams can be computed. An example of a horizontal coverage diagram computed with PETOOL Version 2.0 is presented in Figure 3.6.

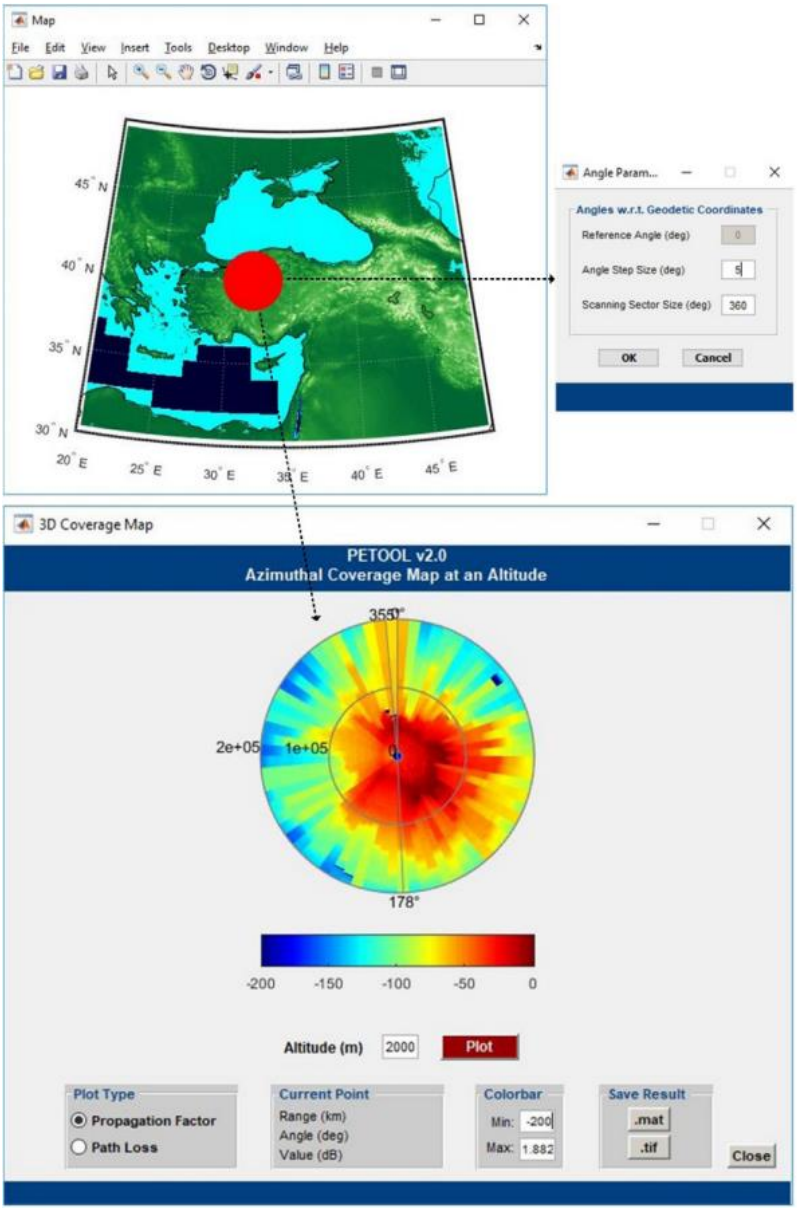

Figure 3.6 Example of an azimuth coverage diagram computed with PETOOL Version 2.0, for a specified altitude (bottom) and the selected terrain elevation map (top).

3.4 Ray-Optics

Whereas the PE method is efficient to characterise the field strength and large-scale parameters, it is difficult to extract precise information about the spread in delay times and the angle-of-arrival. The ray-optics method is applied to calculate the trajectory of each individual ray and model the propagation channel. The ray-optics method has been assessed in more detail using three references. The thesis of Caicedo [24] presents the derivation of the differential equation for the ray trajectory calculation. Caicedo's computations linearize the refractivity index in intervals. This linearization is however unnecessary, since the derivative of the refractivity for each height can be used. This gives a more accurate solution without approximations. The paper of Dinc and Akan [25] presents a statistical large-scale path-loss model for surface-ducts based on the PE simulations and ray-optics to calculate ray trajectories in the presence of a surface duct. Results are presented for spread in delay times, angle-of-arrival and path-losses. Zhou et al. [26] present a detailed description of ray-optics. This reference also provides a comparison of measurements and simulations. This comparison shows that the simulations correspond with the measurements. Comparison of the ray-optics approach of Zhou and results obtained with PETOOL shows that the ray-optics method provides a better path-loss estimate. Because the PETOOL software package is freely available, PETOOL results are widely used as a reference for ray-optics and other simulations.

Ray-optics provides all the variables required for the radar model, specifically the aspect angles and the delay times of the direct and indirect propagation paths. Within the framework of the current project, the ray-optics method has been implemented based on the method of Zhou et al. [26]. This method has been adapted to reduce the computation time. The elevation angle step size must be small for accurate calculation at a great distance. However, due to the propagation, the beam fans out as a function of range, requiring an increasing number of elevation steps. To reduce the computation time, a two-step approach has been implemented: first a coarse ray-optics computation is performed, followed by an interpolation at the desired position. The processing steps in the implemented ray-optics approach are shown in Figure 3.7 and described in detail in the following subsections.

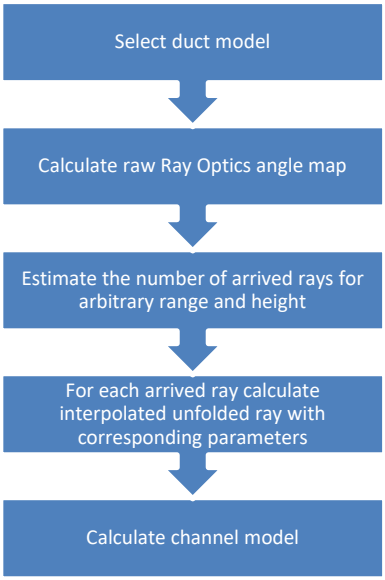

Figure 3.7 Processing steps in the implemented ray-optics approach.

3.4.1 *Duct Model*

The refractive index $n(r,z)$ is a function of the height z and range r. If the refractive index is not range dependent, the range dependency is omitted. The derivative by height is calculated numerically

$$\frac{dn(r,z)}{dz} = \frac{n(r,z+\Delta z)-n(r,z)}{\Delta z}. \tag{3.3}$$

A closed form of the derivative is used if available.

3.4.2 *Ray Trajectory Calculation*

The Eikonal equation describes the ducting wave propagation

$$\frac{d^2z}{dx^2} = K = \frac{1}{r_e} + \frac{1}{n\big(r,z(r)\big)}\frac{dn\big(r,z(r)\big)}{dz}. \tag{3.4}$$

In many cases the first term is negligible. The start conditions are dictated by the transmitted wave at the transmitter antenna with antenna height h_t and transmitter angle θ_t

$$z = \frac{K}{2}x^2 + \theta_t x + h_t. \tag{3.5}$$

Solving this differential equation is performed iteratively, starting with the initial conditions. The height is updated with each range step Δr up to the maximum ground distance or maximum height. The iterative equations are expressed as

$$\alpha\big(z(r)\big) = \frac{1}{n\big(r,z(r)\big)}\frac{dn\big(r,z(r)\big)}{dz}, \tag{3.6}$$

$$z(r+\Delta r) = \frac{\alpha\big(z(r)\big)}{2}(\Delta r + R)^2 + z'(r)(\Delta r + R) + z(r) \tag{3.7}$$

and

$$z'(r+\Delta r) = \alpha\big(z(r)\big)(\Delta r + R) + z'(r). \tag{3.8}$$

The factor R indicates the ground reflection when z lies below the surface. In that case R is the first square-root of the quadratic polynomial in x, smaller than zero

$$\frac{\alpha\big(z(r)\big)}{2}\,x^2 + z'(r)\,x + z(r) = 0 \qquad \text{roots} \qquad x_1, x_2. \tag{3.9}$$

This root steers the differential equation in the opposite direction in case of a surface reflection. In all other cases, R is zero. This process is summarised with the following conditions

$$\begin{aligned} z(r) \geq 0 \;\; \text{then} \;\; R = 0; \\ z(r) < 0 \;\; \text{then} \;\; R = \min(x_1, x_2). \end{aligned} \tag{3.10}$$

In case of a reflection, the derivative changes sign and the wave is discontinuous. By counting the number of reflections, $N_r(r)$ the unfolded ray $z_u(r) = (-1)^{N_r(r)} z(r)$ can be determined which is continuous with positive and negative values. Discontinuities have the disadvantage that interpolation is not possible, it causes unreliable results for the interpolated rays around the reflection point. In case of a range-independent refractivity index, the duct patterns repeat. When a duct pattern from a reflection to subsequent reflection is known, it is repeated up to the maximum distance. This step reduces the computation time and has similarities with the method of Zhou et al. [26]. Other advantages are that all rays are available for varying distances and the entire propagation path is available.

The result of this step is the ray-optics angle map $z_u(\theta_t, r)$. This map indicates the expanded height as a function of transmission angle and distance and serves as a starting point for further calculations.

3.4.3 Ray Interpolation

The purpose of this step is to calculate the channel model at a specified distance r_{select} and height h_{select}. No matter how fine the elevation grid is, the chance that the rays calculated in the previous step pass exactly through this point is very slim. After the intersections have been determined, the interpolated rays and transmission angles are calculated. Linear interpolation produces sufficiently accurate results. Due to the unfolded rays, the intersections with positive and negative height are estimated

$$\begin{aligned} z_u\big(\theta_{t,i}, r_{\text{select}}\big) < h_{\text{select}} \leq z_u\big(\theta_{t,i+1}, r_{\text{select}}\big); \\ z_u\big(\theta_{t,i}, r_{\text{select}}\big) < -h_{\text{select}} \leq z_u\big(\theta_{t,i+1}, r_{\text{select}}\big). \end{aligned} \tag{3.11}$$

The result of this step is a set of M interpolated arrived rays $z_{u,m}(r)$ and corresponding transmission angles $\theta_{t,m}$. The arrived angle is the numerical difference of the last two values

$$\theta_{a,m} = \tan^{-1}\left(\frac{z_{u,m}(r_{\text{end}}) - z_{u,m}(r_{\text{end}-1})}{\Delta r}\right). \tag{3.12}$$

The grazing angle is the derivative located at zero height of the unfolded ray

$$\theta_{g,m} = \tan^{-1}\left(\frac{z_{u,m}(r_{\text{zero}}) - z_{u,m}(r_{\text{zero}-1})}{\Delta r}\right). \tag{3.13}$$

The path length and electrical length are according the Pythagorean Theorem

$$L_{\text{path},m} = \sum_{i=2}^{i_{\text{end}}} \sqrt{\Delta r^2 + \left(z_{u,m}(r_{\text{i}}) - z_{u,m}(r_{\text{i-1}})\right)^2} \tag{3.14}$$

and

$$L_{\text{electrical},m} \approx n(0) \sum_{i=2}^{i_{\text{end}}} \sqrt{\Delta r^2 + \left(z_{u,m}(r_{\text{i}}) - z_{u,m}(r_{\text{i-1}})\right)^2}. \tag{3.15}$$

The electrical length is an approximation suitable for this research, see [24] for another more extensive approximation.

3.4.4 Channel Model

The channel model takes the form as introduced in [26], [27]. The channel model is

$$H_m = \sqrt{\frac{P_t G_t L_t}{4\pi L_{electric,m}^2}}\beta_m e^{j\left(\frac{2\pi f_c L_{electrical,m}}{c} + \lambda_m \pi + \phi\right)} e^{j2\pi D_0 t}, \qquad H_{radio} = \sum_{m=1}^{M} H_{radio}, \tag{3.16}$$

$$\beta_m = \beta_0 \gamma_1 \gamma^{\lambda_m - 2} \gamma_N, \tag{3.17}$$

$$\beta_0 = \frac{1}{\sum_{m=1}^{M} \beta_m}, \tag{3.18}$$

and

$$D_0 = \frac{v f_c \cos(\theta_0)}{c}, \tag{3.19}$$

where M is the number of arrived rays on the receiver, m is the ray index, P_t is the transmitted power, G_t is the transmitter antenna gain, L_t is the transmitter losses, β_m is the normalised path gain, f_c is the carrier frequency, L_m is the electrical path length, λ_m is the number of surface reflections, ϕ is a random phase shift, γ is the

reflection coefficient and D_0 is the Doppler shift due to the sea surface motion. The transmitted power and transmitter antenna gain are only scaling constants, thus they can be neglected for a first order analysis. The reflection coefficient depends on the type of surface. The reflection coefficient of the rough sea surface is used

$$\gamma = S_a^2 D_v \Gamma e^{-8\left(\frac{\pi h_0 \cos(\alpha)}{\lambda}\right)^2}, \tag{3.20}$$

where S_a is the shadowing factor, D_v is the divergence factor, Γ is the reflection coefficient, h_0 is the sea surface height and α is the incident angle. A good approximation of the divergence valid under a large number of scenarios is [28]

$$D_v \approx \frac{1}{\sqrt{1+\frac{4r_1 r_2}{r_e r \sin(\theta_g)}}}, \tag{3.21}$$

in which $r_1 + r_2 = r$ and r_1 are the earth distance of the transmitter to the reflection point on earth, r_2 is the earth distance of the receiver to the reflection point and θ_g is the grazing angle. Parsons [29] and CARPET [14] describe similar divergence equations with almost equivalent results. Note that the first and last reflection coefficients γ_1 and γ_N differ from the intermediate values, demanding some manipulation in case of a single reflection. The normalised path gain is one in case of no reflection. The radio path losses can be written as

$$PL(d) = -10\ \log_{10}\left(|H_{radio}|^2 G_r L_r \frac{\lambda^2}{4\pi}\right), \tag{3.22}$$

where d is the average range, G_r is the receiver antenna gain, and L_r are the receiver losses. The path losses are displayed independently of the constant radar parameters which are just a scaling factor. This means that the transmitter power, transmitter antenna gain, transmitter losses, receiver antenna gain and receiver losses are set to one.

The channel model provides the one-way propagation between two points. Radar systems have two-way propagation form the transmitter to target and from target to receiver. The two-way channel model is a modified version of the one-way channel model defined in (3.16) through (3.19)

$$H_{radar} = \sum_{m_1=1}^{M}\sum_{m_2=1}^{M}\sqrt{\frac{P_t G_t L_t}{4\pi L_{electric,m_1}^2}}\sqrt{\frac{G_r L_r}{4\pi L_{electric,m_2}^2}}\ \beta_{m_1}\beta_{m_2} \\ e^{j\left(\frac{2\pi f c\left(L_{electrical,m_1}+L_{electrical,m_2}\right)}{c}+(\lambda_{m_1}+\lambda_{m_2})\pi+\phi\right)} e^{j2\pi D_0 t}, \tag{3.23}$$

$$\beta_m = \beta_0 \gamma_1 \gamma^{\lambda_m - 2}\gamma_N, \tag{3.24}$$

$$\beta_0 = \frac{1}{\sum_{m_1=1}^{M}\sum_{m_2}^{M}\beta_{m_1}\beta_{m_2}}, \tag{3.25}$$

and

$$D_0 = \frac{v\, f_c \cos(\theta_0)}{c}. \tag{3.26}$$

In radar systems, the total number of rays is M^2, assuming M possible rays from the transmitter to the target and M possible rays from the target to the receiver. The radar channel model is very similar to a multiple-input/multiple-output (MIMO) radar system description by Godrich et al. [30]. Godrich's model is more general and assumes that the number of transmitters is not equal to the number of receivers. The radar path losses can be written as

$$PL(d) = -10\ \log_{10}\left(|H_{radar}|^2 \frac{\lambda^2}{4\pi}\right), \tag{3.27}$$

where d is the average range. We assume that the constant radar system parameters are set to one.

3.4.5 Radar Measurements and Actual Values

In case of ducting, the overall signal received from a target is the coherent combination of the rays arriving at the receiver via various paths, to and from the target. Therefore, depending on the geometry, the measured target's range, elevation and radial velocity differ from the actual values. In addition, the power of the received signal will vary as the path lengths change due to a target moving or small variations in the environment. These effects are assessed in the following subsections.

3.4.5.1 Range

All reflections are added coherently in the receiver. The range bin corresponding to the maximum power is the target's range estimate. After pulse-compression the range response has pattern $\Psi_r(\mathrm{r})$. An example range response pattern is the sinc function scaled with the range resolution Δr

$$\Psi_r(\mathrm{r}) = \sin(r/\Delta r)/(r/\Delta r). \tag{3.28}$$

The coherent addition in the receiver is the sum of the received responses multiplied with the complex propagation factors p_m. After the receiver, the range with the maximum value is selected

$$P_r(r) = \sum_{m=1}^{M} p_m \Psi_r\left(L_{electrical,m} - r\right), \tag{3.29}$$

$$L_{electrical,m} = L_{electrical,m_1} + L_{electrical,m_2} \tag{3.30}$$

and

$$\hat{L}_{electrical} = max_r(|P_r(r)|), \tag{3.31}$$

where M is the number of propagation paths and $\hat{L}_{electrical}$ is the arrival electrical path length belong to the M paths. An approximation of this value is the weighted electrical length assuming the sinc function is one. The weighted electrical range mean and square of the standard error depends on the signal strength

$$\hat{L}_{electrical} = \frac{\sum_{n=1}^{N} L_{electrical,n}|\beta_n|}{\beta_s}, \tag{3.32}$$

$$\beta_s = \sum_{n=1}^{N} |\beta_n| \tag{3.33}$$

and

$$\sigma^2_{\hat{L}_{electrical}} = \frac{N}{(N-1)\beta_s^2} \sum_{n=1}^{N} |\beta_n|^2 \left(L_{electrical,n} - \hat{L}_{electrical}\right)^2. \tag{3.34}$$

The range rate is the difference of succeeding range measurements in a specific time interval ΔT. This function is supposed to be represented with a linear dependency

$$L_{electrical}(t) = L_{electrical,0} + \frac{dL_{electrical}(t)}{dt} t, \tag{3.35}$$

where $L_{electrical,0}$ is the offset electrical length and $dL_{electrical}(t)/dt$ is the range rate. A linear least squares fit around with samples in the window ΔT gives the values corresponding this linear equation.

3.4.5.2 Radial Velocity

Radar systems derive the radial velocity of a target from the pulse to pulse phase change of the target response. This phase change is affected by variations of the actual electrical path lengths of the different rays arriving from the target at the receiver. This is effect not covered here and requires further study.

3.4.5.3 Elevation

The elevation angle is calculated with a beamformer algorithm, the complex values of the propagation factors p_m are multiplied with the beamformer coefficients with antenna pattern $\Psi_a(\theta)$ and the angle with maximum value is selected

$$P_a(\theta) = \sum_{m=1}^{M} p_m \Psi_a(\Theta_m - \theta_e - \theta), \tag{3.36}$$

where

$$\hat{\theta} = max_{\theta}(|P_a(\theta)|), \tag{3.37}$$

in which M is the number of propagation paths, θ_e is the antenna elevation angle and θ_m the arrival elevation angles belong to the M paths.

Here a distinction is made between the transmission angle $\hat{\theta}_t$ and the angle-of-arrival of a one-way receiver angle $\hat{\theta}_{a1}$ at the target location or a two-way receiver angle $\hat{\theta}_{a2}$.

3.4.5.4 Received Power

The path losses differ across the propagation areas, the range dependency depends on the distance travelled that deflects during propagation. A function that reflects this is the received power

$$P(r) = P_0 + \frac{dP(r)}{dr}r, \tag{3.38}$$

where P_0 is the offset power and $dP(r)/dr$ is the derivate with respect to the range. A linear least squares fit around a selected range r_{select} with samples in the range window ΔR, $r_{select} - \frac{1}{2}\Delta R < r \leq r_{select} + \frac{1}{2}\Delta R$, gives the values corresponding to this linear equation. The window ΔR is chosen in such a way that there is a good averaging.

3.4.6 Results and Validation

In this section, the ray-optics results are compared to Zhou's results described in [26]. Zhou present results for a relative easy linear refractive index. The altitude lies between 0 m and 60 m. The solution of the differential equation stops above 60 m.

Figure 3.8 presents folded and unfolded rays. The unfolded rays do not have discontinuities and interpolation can therefore be performed without errors. Figure 3.9 shows the entire raw ray-optics angle map. The raw ray-optics angle map presents information about the number of surface reflections. Figure 3.10 shows the number of reflections. With the number of reflections you can easily switch from folded to unfolded rays. Figure 3.11, the last figure of this sequence, presents the number of reflections for specific heights. This figure can be compared with a similar figure in Zhou's [26] paper. The number of arrived rays is the same.

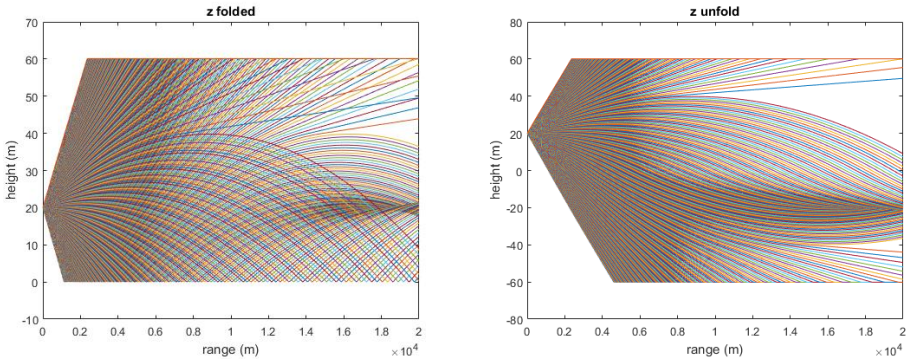

Figure 3.8 The ray-optics results (left) and the unfolded results (right).

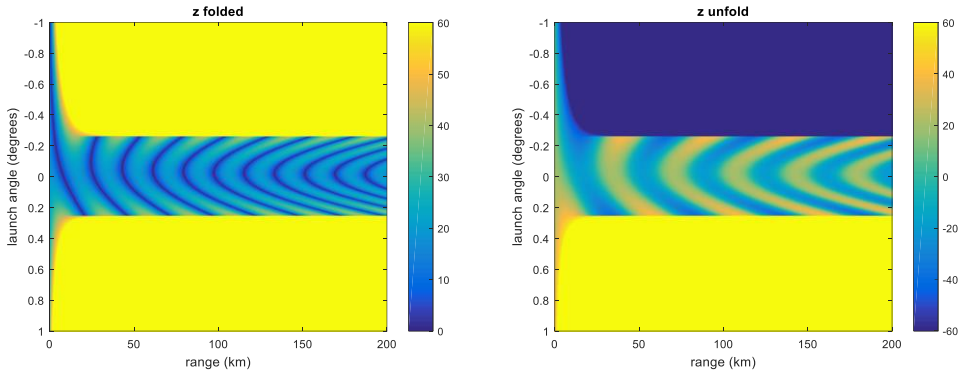

Figure 3.9 The folded ray-optics angle map (left) and the unfolded ray-optics angle map (right).

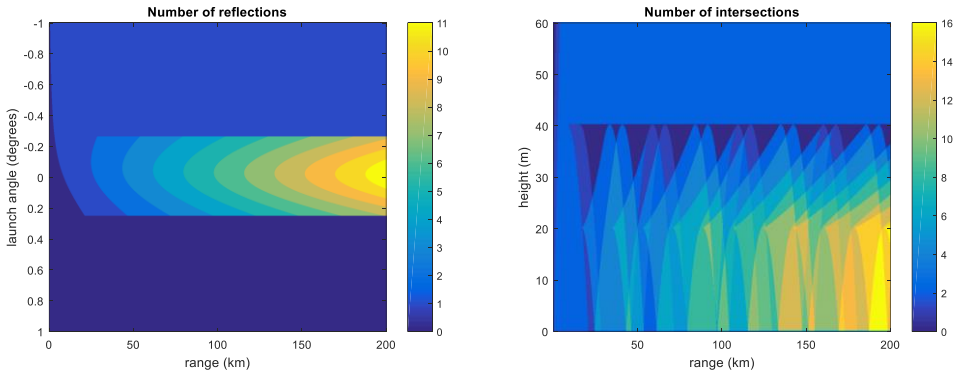

Figure 3.10 Number of reflections in the raw ray-optics angle map (left) and the number of arrived rays (right).

The ray-optics method provides more insight into wave propagation than the PE results. All results should be reviewed closely and can be summarised as follows:

- The results are consistent with Zhou et al. [26].
- The measured elevation angle to a target fluctuates widely in the duct area.
- The path losses show a discontinuity around the trapping angle. Targets below the trapping angle in the ducting area have a greater path loss than targets above the ducting height.
- The path losses in the duct area show greater variations than above the duct area due to the constructive and destructive summation in the receiver.
- In principle, all propagation problems can be solved with ray-optics. However, a brute-force method is needed to find the actual propagation path(s) between two given positions (e.g., the radar system and a target).

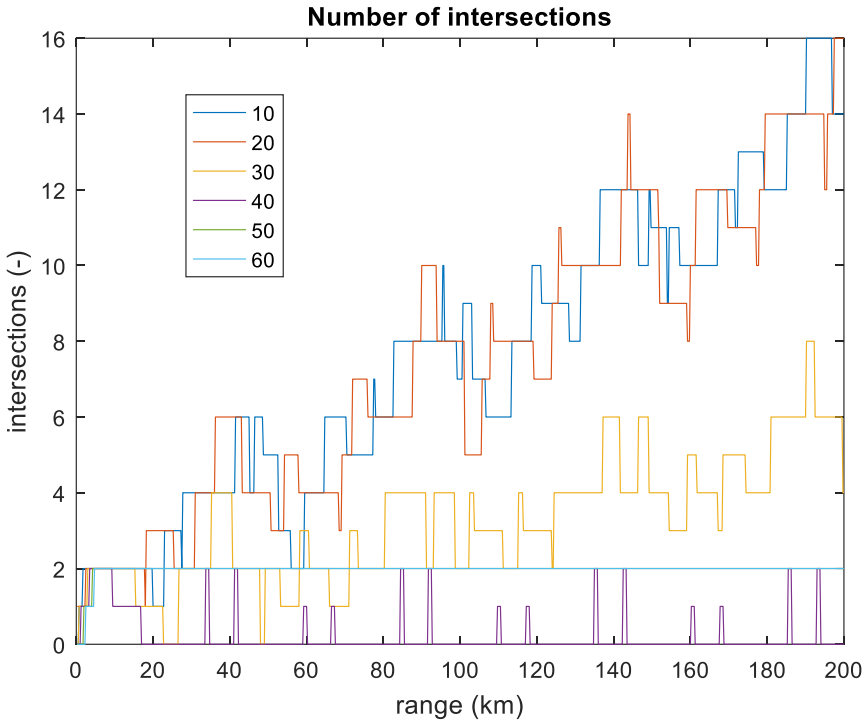

Figure 3.11 Number of arrived rays for receivers on 10, 20, 30, 40, 50 m height.

4 Assessment and Correction of Propagation Effects

In Chapter 2, the effects of anomalous propagation on radar performance have been discussed. The effects can be severe, ranging from a significant increase of the detection distance to regions where the probability of detection diminishes. As a consequence, awareness of the current propagation conditions is crucial to assess and predict the radar performance and to identify possible regions where the detection probability may be degraded. The current radar performance can be assessed with the aid of propagation models, such as the models introduced in Chapter 3. The accuracy of a propagation model depends directly on how well the refractivity profile is measured or modelled [13], [11]. This, in turn, depends on the accurateness of the atmospheric data used to feed the model. In Section 4.1, the requirements with respect to the atmospheric input data are discussed.

Subsequently in Section 4.2, it is discussed how atmospheric data can be obtained and used on board a platform on sea. The expected accurateness of the data is considered as well.

In general, on board a platform on the open sea, it will be difficult to gather all data necessary to run propagation models with the required accurateness. Therefore, it would be very valuable if current effects of propagation could be extracted from radar measurements and then used for correcting measurements, i.e., without the need for running propagation models. The feasibility of this idea is investigated for two different approaches. In the first approach, it is assumed that radar measurements in just a single frequency band are available. This approach is explained and analysed in Section 4.3. In the second approach, discussed in Section 4.4, multiband radar measurements are exploited to estimate and correct propagation effects. This latter approach is of special interest for the integrated XS-Suite and the future integrated LSX-Suite [31].

4.1 Atmospheric Data Requirements

The accurateness of atmospheric data is determined by the measurement accuracy and the spatial and temporal grid on which the data are available. The required grid size (spatial and temporal) depends on the prevailing weather conditions, the location and field of view of the radar system, the operating radar frequency and the radar performance parameters to be assessed. In general, assessing the radar positioning accuracy requires higher accurateness than assessing the radar coverage and maximum detection distance.

The performance assessment will be more accurate if the atmospheric data are provided on a finer grid (spatial and temporal). For an accurate radar performance prediction (i.e., propagation loss prediction) at 10 GHz, the recommended vertical and horizontal grid size at which the atmospheric data have to be provided is of the order of 6 to 10 m and 17 km respectively [2]. To maintain an accurate performance prediction, the atmospheric data should be updated every two to four hours [2], [13]. In more turbulent weather conditions, the required update period is one hour or even less.

For radar coverage and detection distance assessment, on the other hand, the assumption of a stratified atmosphere using a single vertical refractivity profile may be adequate for as long as 24 hours [2], if the atmosphere and weather conditions are steady.

4.2 Obtaining Atmospheric Information

In this section, it is discussed how atmospheric information can be obtained and used on board a platform. Onboard sources for atmospheric data are existing databases, (commercial) weather services and dedicated measurement equipment.

4.2.1 Long-Term Averaged Atmospheric Data

Over the years many measurements have been performed of the atmosphere. These long term measurements yield average refractivity profiles. One example of an extended database of long-term atmospheric profiles is the database provided by the International Telecommunication Union (ITU) related to the Recommendation ITU-R P.835-6 [32]. This database includes monthly averages of vertical profiles of temperature, pressure and relative humidity for 353 location spread over the world. This ITU database is freely available [33].

In the propagation models, long-term average refractive profiles might be used instead of the Standard Atmosphere. However, for accurate radar performance prediction, the atmospheric data should be updated every two to four hours and in turbulent conditions even more often. Consequently, using long-term average refractivity profiles will not suffice for accurate radar performance prediction in the more fluctuating lower-air layer.

See Appendix A for an extended discussion of the ITU-R P.835-6 database.

4.2.2 Weather Prediction Models

With the aid of numerical weather prediction (NWP) models, the upper-air vertical refractivity profile can be computed on a grid of points. The information needed to feed NWP models can be meteorological data gathered worldwide by radiosondes, ships, buoys, aircraft and satellites. However, in practice it may be difficult to timely collect all these data on board a platform on the open sea.

For computing the average lower-air refractivity profile, extending up to 50 to 300 m altitude depending on the atmospheric stability, empirical models have been developed requiring sea-surface temperature, air temperature, pressure and humidity as inputs. These inputs can be obtained using standard measurement equipment, such as a thermometer and anemometer.

The results of NWP models are sufficiently detailed to provide an indication of the radar coverage under the prevailing weather conditions according to [2]. NWP models neglect however fine-scale atmospheric and temporal variations. To correct range and elevation errors of radar measurements, higher accuracy and resolution are required.

4.2.3 In Situ Measurements

On board a platform on the open sea, the means to gather accurate information about the atmosphere are however limited. One way of acquiring information on the

atmosphere are in-situ measurements by means of a radiosonde balloon. The main disadvantage is that a radiosonde measurement provides the vertical refractivity profile for just a single point close to the platform. To obtain atmospheric information in a larger area, radiosondes may be deployed by an aircraft. In that case, the radiosondes are deployed at high altitude and descend by parachute. In practice, this is however cumbersome, time consuming and costly [2].

Specific sensors may be brought on board to characterise the atmosphere. It is however improbable that atmospheric information can be obtained with the required accuracy and resolution using a single sensor modality [34]. Consequently, a variety of sensors should be installed on board just for atmospheric measurements, e.g., an acoustic echo sounder, lidar and radiometer. In [2] it is stated that the resolution and accuracy of such sensors is presently insufficient for accurate assessment and prediction of radar propagation, but atmospheric remote sensing techniques are in continuous development.

All things considered, it would be advantageous if the current effects of propagation could be extracted from radar measurements. In that case there is no need to bring additional sensors on board the platform, data can be obtained within the whole radar volume and there might be methods to directly correct radar measurements without the need for generating refractivity profiles and running propagation models. In the following two sections, different examples are given and analysed of how radar measurements can be exploited to assess and correct the effects of propagation.

4.3 Single-Frequency Radar Measurements

In this section five scenarios are introduced explaining how single-band radar measurements can be exploited for assessing and correcting propagation effects. For this approach, using single-band radar measurements, a reference is needed. Such a reference could be (steady) clutter, a ‘cooperative’ target with known position or other radio-frequency signals. Finally, the effectiveness of this approach is evaluated, assuming a cooperative target with known position is present within the radar volume.

4.3.1 Scenario 1: Surface Clutter

Some examples of extracting information about the propagation conditions or the refractivity profile have already been reported in literature. One example is the observation of (sea) clutter reflections at long range, which is an indication that the radar waves are trapped in a ducting layer [18]. In Figure 4.1 an example is shown where sea clutter reflections are observed for extended ranges if a surface-based duct is present.

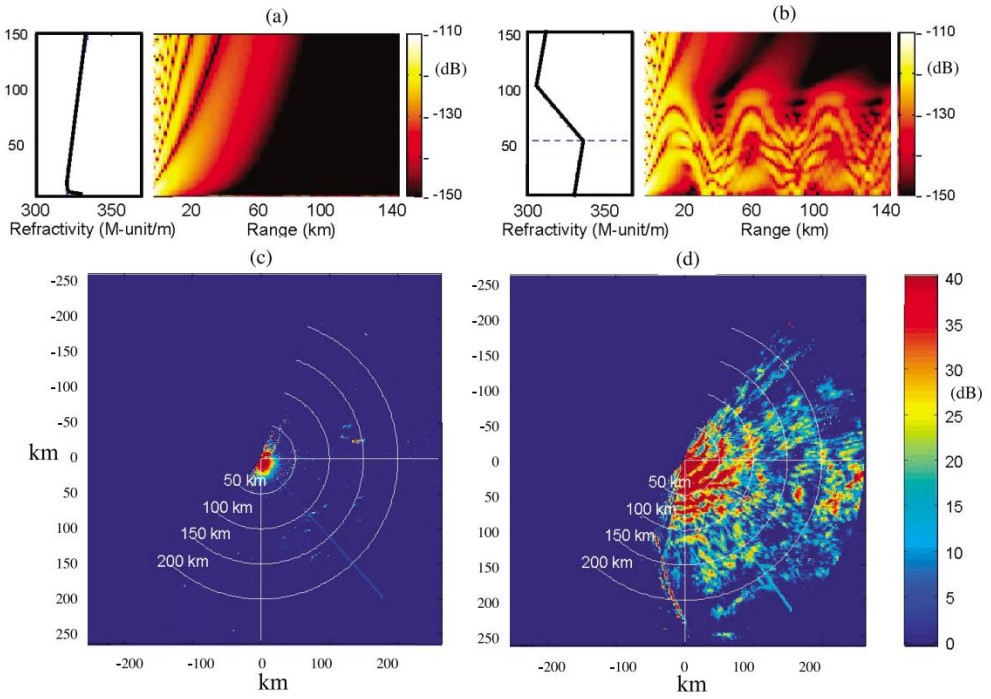

Figure 4.1 Examples of radar plan position indicator (PPI) plots showing the clutter map for a weak evaporation duct (left) and a surface-based duct (right). By courtesy of [35].

If the measurement geometry is known, the height of the ducting layer can be extracted from the observed so-called *clutter rings*. By assuming a model for the refractivity profile as function of height (e.g., piece-wise linear), it is feasible to estimate the range-dependent refractivity profile from clutter-ring observations [36], [37]. Observing clutter rings, could be a trigger to adapt the radar waveform settings as suggested in Section 1.2. Since, due to ducting, the radar waves travel further than expected, the clutter responses may become ambiguous in range decreasing the signal-to-clutter ratio within the unambiguous range interval. To mitigate this effect, a radar waveform with lower pulse repetition frequency can be selected, enlarging the unambiguous range interval. (Whether it is indeed feasible to select a waveform with lower pulse repetition frequency depends on the actual operational situation.)

In case of stationary ground targets, the phase of the received echoes can be exploited to extract the near-surface refractivity [38]. For this method to be accurate, the ground targets need to be stationary and persistent, their radar cross section should be relatively high and they should not have moving parts. This method may possibly be applied in the littoral environment if stationary targets on land can be observed with the radar. However, the movements of the own platform need to be carefully compensated for.

4.3.2 Scenario 2: Satellites with Known Orbit

This first scenario considers tracking of targets at long range and relatively low elevation, e.g., ballistic missiles. Due to the low elevation of the target, the propagation path through the atmosphere is long (even if the target itself is outside the Earth's atmosphere). If the ballistic missile is inside the atmosphere, the track accuracy should be sufficient to estimate the missile's drag coefficient. As a consequence, the influence of the atmosphere on the radar wave propagation,

needs to be compensated adequately for the drag coefficient to be accurately estimated.

To obtain an indication of the influence of the atmosphere on the radar wave propagation in this case, low Earth orbit (LEO) satellites or calibration satellites, e.g., [39], [40], can be exploited, provided the orbits are known with sufficient accuracy. By tracking the satellites at low-elevation angles, the elevation measured with the radar can be compared to the elevation as computed from the known orbit. The difference can be used as a simple correction on the measured elevation.

4.3.3 Scenario 3: Cooperative Targets

Multiple radar systems, operating in a radar network, may observe the same target from different aspect angles and ranges. To improve the overall, joint track accuracy, the plots (position and velocity estimates) obtained by the individual radar systems within the network, need to be fused. However, due to the different locations of the radar systems, the measurements of the individual systems are influenced by the atmosphere in different ways. Depending on the network geometry and the atmospheric circumstance, the radar plots need to be corrected before they can be fused in a tracker.

Similar to the previous scenario, a cooperative target can be exploited to extract information on the influence of the atmosphere. For instance an airliner providing reliable and sufficiently accurate Automatic Dependent Surveillance-Broadcast (ADS-B) information, can be used to estimate the error in the radar measurements [41].

A special radar mode which is applicable for a radar network is the bistatic radar mode. In this mode one radar system transmits while one or more radar systems receive the reflections from the environment. As the path from the transmitter to the target and the various paths from the target to the receivers are all different, multiple paths are simultaneously sampled with a single transmission.
Also, depending on the geometry, the direct-path signal, going directly from the transmitter to a receiver, can be obtained. By exploiting such a set of measurements, it may be feasible to estimate the refractivity profile assuming a simple atmospheric model (refer to, e.g., [42]).

4.3.4 Scenario 4: Own Assets

In line with the two previous scenarios, an own asset can be exploited to provide ground truth. This can be an organic asset, under control by the platform, such as a small unmanned aerial vehicle (UAV). The UAV may fly a dedicated pattern, while being tracked by the radar system. In particular, radar measurements of the UAV flying at different altitudes, can be used to extract information on duct profiles. For measurements at long ranges the UAV might carry an active transponder.

Depending on the demands of the radar, the asset is required to fly at a certain (high) altitude and therefore not all organic assets might be suitable. Therefore, instead of an organic asset other cooperative assets may be exploited such as a medium altitude, long endurance (MALE) UAV or a patrol aircraft.

4.3.5 Scenario 5: Signals of Opportunity

In the final scenario signals of opportunity are considered. For instance, Global Navigation Satellite System (GNSS) or Global Positioning System (GPS) signals might be used for estimating the influence of the atmosphere, e.g., [1], [43] and references therein. In a coastal environment (persistent) transmitters on land might be used, e.g., [34], [44]. For the use of transmitters on land it is assumed that several transmitters are present, allowing for compensation of the atmospheric effects.

4.3.6 Scenario Analysis

In this section, the effectiveness of using single-band radar measurements of a cooperative target to estimate elevation corrections, is evaluated. The position of the cooperative target is assumed to be known with sufficient accuracy. This evaluation is representative for the scenarios 2 through 4 as defined in the previous sections.

In literature similar methods have been reported [41], [42]. These methods try to estimate the actual propagation parameters and generate the refractivity profile (assuming a simple model). Within the current study, however, the aim is to find a more direct method for correcting radar measurements, without the need for estimation of the refractivity profile. If the actual position $s = (r, \theta, \varepsilon)$ in spherical coordinates and the measured position $s^m = (r^m, \theta^m, \varepsilon^m)$ of the cooperative target are known, the difference between the two can be used to estimate the elevation error, possibly also for targets in other positions.

The first step in the correction procedure is the 4/3 Earth-radius correction

$$s^e = F_{\frac{4}{3}}(s). \tag{4.1}$$

The 4/3 Earth-radius correction is related to the refractive index with altitude. For this correction an average refractive index is used. The difference between the actual and measured target positions, can be expressed in spherical or in Cartesian coordinates [42]. The correction is preferably performed in spherical coordinates

$$\Delta s(s, s^m) = \begin{pmatrix} \Delta r(r, \theta, \varepsilon) \\ \Delta\theta(r, \theta, \varepsilon) \\ \Delta\varepsilon(r, \theta, \varepsilon) \end{pmatrix} = F_{\frac{4}{3}}(s) - s^m. \tag{4.2}$$

For a target in another position, the same correction factor can be applied. The correction is a function of the actual position of that target $s^i = (r^i, \theta^i, \varepsilon^i)$.

If it is assumed that the propagation conditions are stationary in azimuth, the azimuth correction can be neglected. The required range correction is typically small and negligible compared to the elevation correction. The elevation correction factor is a function of the target range. The elevation correction ε^c is therefore weighted with the range in case of a single cooperative target

$$\varepsilon^c(s^i) = \frac{r^i}{r}\Delta\varepsilon(s, s^m) = \frac{r^i}{r}\left(\varepsilon_{\frac{4}{3}} - \varepsilon^m\right). \tag{4.3}$$

When multiple cooperative targets are present or multiple measurements on a single target are present, a correction function with more degrees of freedom and corresponding parameters can be designed.

For the quantitative analysis, the complex propagation factors and associated elevation angles are calculated with TERPEM, assuming three radars on the North Sea in the X-band, S-band and L-band. The radar height is 30 m, tilt angle 3° and 6° beamwidth. The -3 dB points lies on the horizon. A cooperative target is assumed to be present in either position **A** or position **B**, as indicated in the elevation error as function of the target position of the individual radar bands. The elevation error associated with either one of these positions, has been used to correct the measured elevation for all other grid points of the defined height-range grid. The histograms are shown of the remaining elevation errors using the Standard Atmosphere, the averaged profile of the ITU-R P.453-11 database and a single profile of the ITU-R P.835-6 database (see Appendix A), respectively. The histogram values corresponds with the range-height values in the radar beam.

4.3.6.1 X-band radar

This section presents the cooperative target results for an X-band radar.

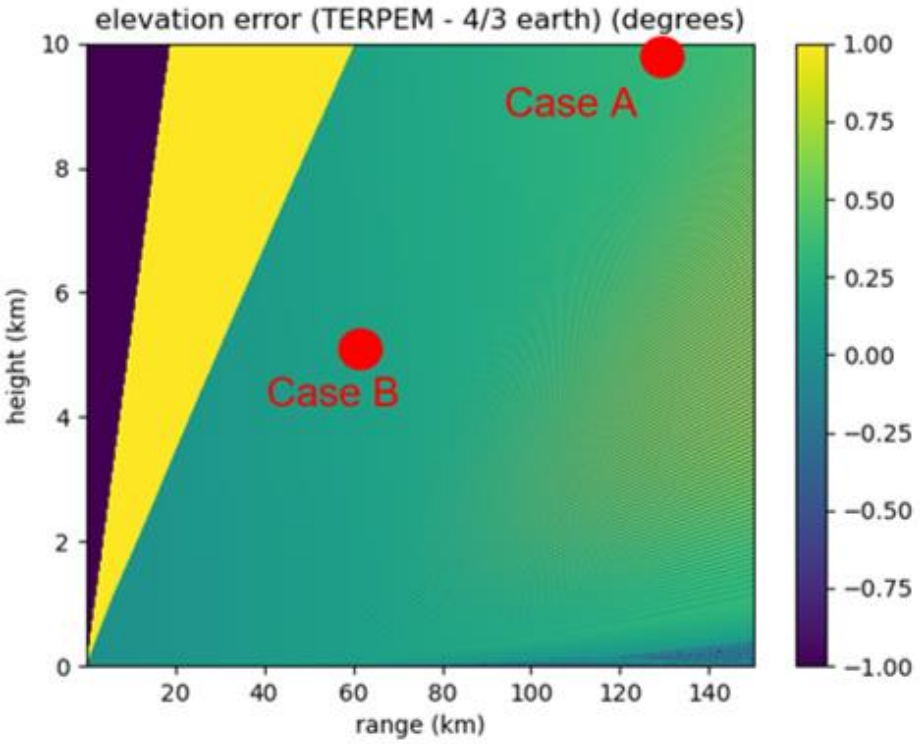

Figure 4.2 X-band radar elevation error as function of target location computed using the standard refractivity profile, with the two different positions of the cooperative target, **A** and **B**. The colour denotes the elevation error in degrees.

The elevation error in Figure 4.2 shows fine fluctuation around multipath nulls. The fluctuations are fine due to the small wavelength. Above the 4.5° elevation angle (the line from the origin to the upper left corner) lie no multipath fluctuations.

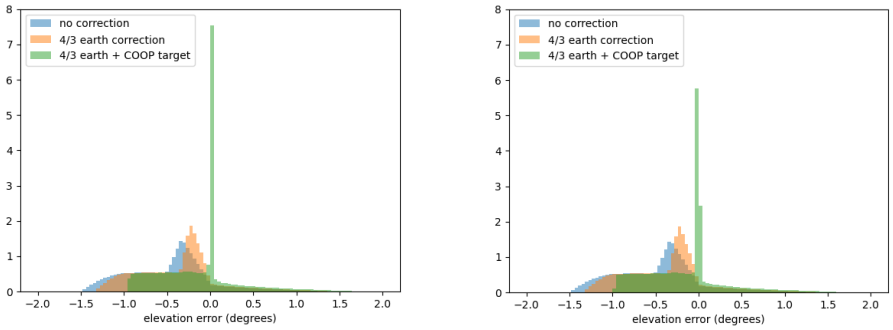

Figure 4.3 X-band radar histogram of the elevation error without correction, 4/3 Earth-radius correction and with the additional cooperative target correction with the Standard Atmosphere. On the left the histogram when the cooperative target is in position **A** and on the right the histogram when the cooperative target is in position **B**.

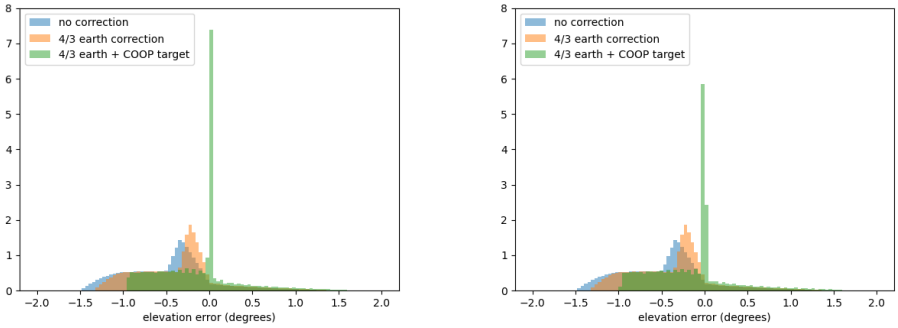

Figure 4.4 X-band radar histogram of the elevation error without correction, 4/3 Earth-radius correction and with the additional cooperative target correction using the average profile from the ITU-R P.453-11 database (North Sea). On the left the histogram when the cooperative target is in position **A** and on the right the histogram when the cooperative target is in position **B**.

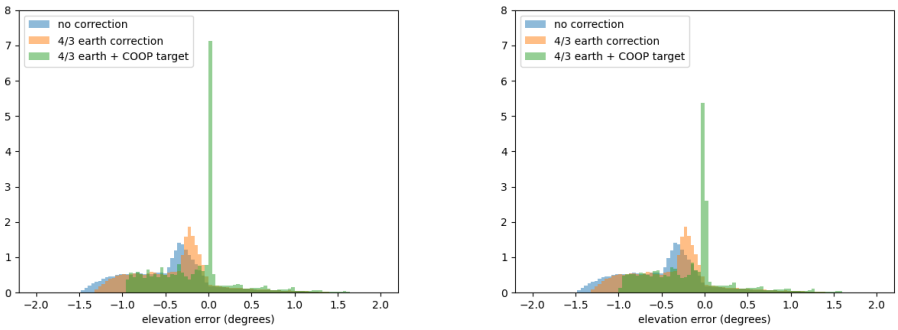

Figure 4.5 X-band radar histogram of the elevation error without correction, 4/3 Earth-radius correction and with the additional cooperative target correction with a single profile from the ITU-R P.835-6 database. On the left the histogram when the cooperative target is in position **A** and on the right the histogram when the cooperative target is in position **B**.

The histograms of the elevation error show that the 4/3 Earth-radius correction shifts the histogram to zero: it is a first-order correction. The cooperative target correction shifts the entire histogram to zero and narrows the histogram peak. The elevation errors are concentrated around zero. The histograms show that this

correction can only be applied outside the propagation zeros. The two cases show that the applied method gives smaller elevation errors in the region without multipath.

4.3.6.2 S-band radar

This section presents the cooperative target results for an S-band radar.

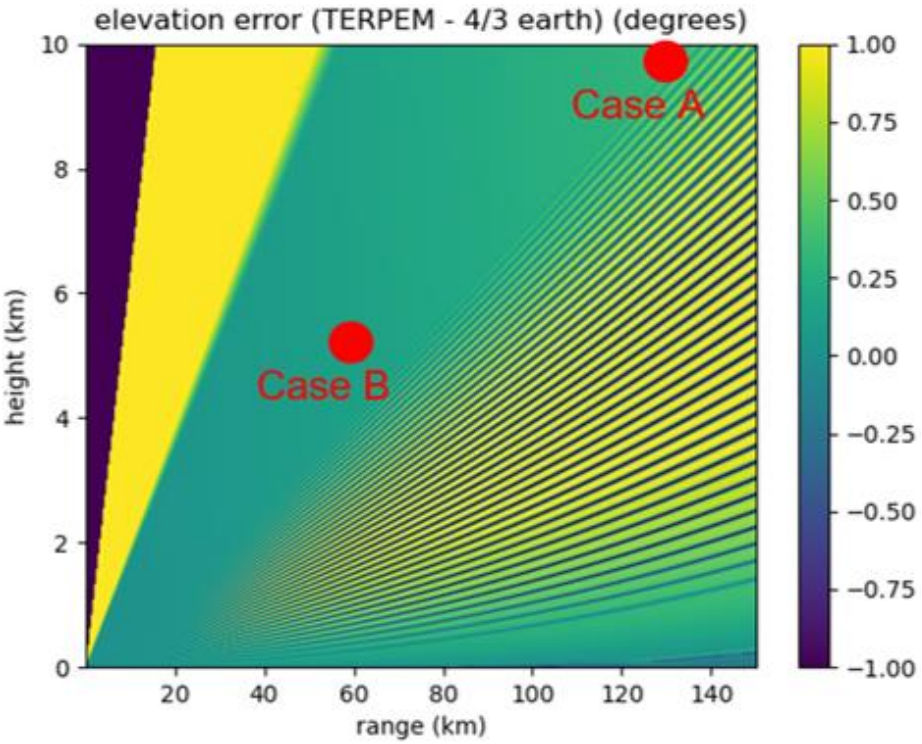

Figure 4.6 S-band radar elevation error as function of target location computed using the standard refractivity profile, with the two different positions of the cooperative target, **A** and **B**. The colour denotes the elevation error in degrees.

The elevation shows fluctuation around multipath nulls. The fluctuations are not as fine compared with the X-band radar due to the larger wavelength. Above the 4.5° elevation angle (the line from the origin to the upper left corner) lie no multipath fluctuations.

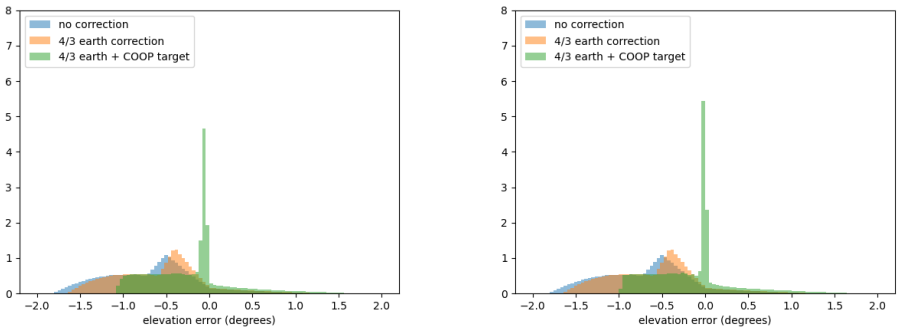

Figure 4.7 S-band radar histogram of the elevation error without correction, 4/3 Earth-radius correction and with the additional cooperative target correction with the Standard Atmosphere. On the left the histogram when the cooperative target is in position **A** and on the right the histogram when the cooperative target is in position **B**.

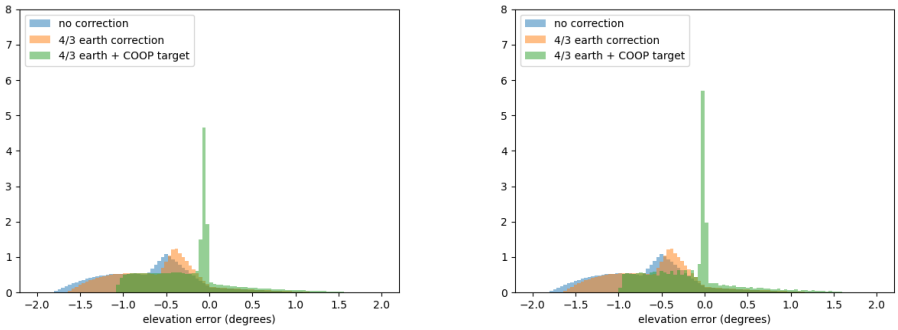

Figure 4.8 S-band radar histogram of the elevation error without correction, 4/3 Earth-radius correction and with the additional cooperative target correction using the average profile from the ITU-R P.453-11 database (North Sea). On the left the histogram when the cooperative target is in position **A** and on the right the histogram when the cooperative target is in position **B**.

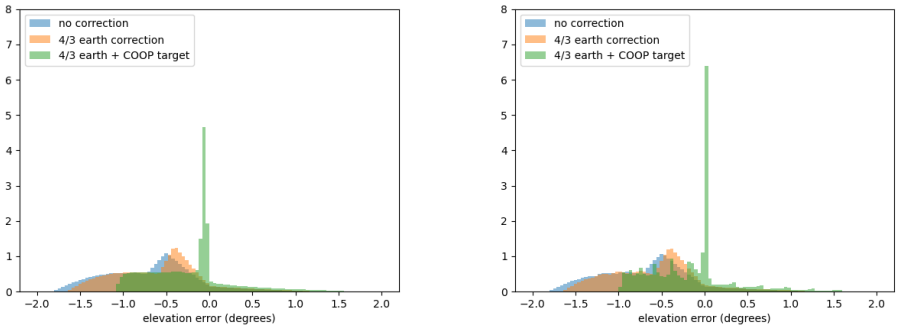

Figure 4.9 S-band radar histogram of the elevation error without correction, 4/3 Earth-radius correction and with the additional cooperative target correction with a single profile from the ITU-R P.835-6 database. On the left the histogram when the cooperative target is in position **A** and on the right the histogram when the cooperative target is in position **B**.

The histograms show the same characteristics as the X-band radar.

4.3.6.3 L-band radar

This section presents the cooperative target results for an L-band radar.

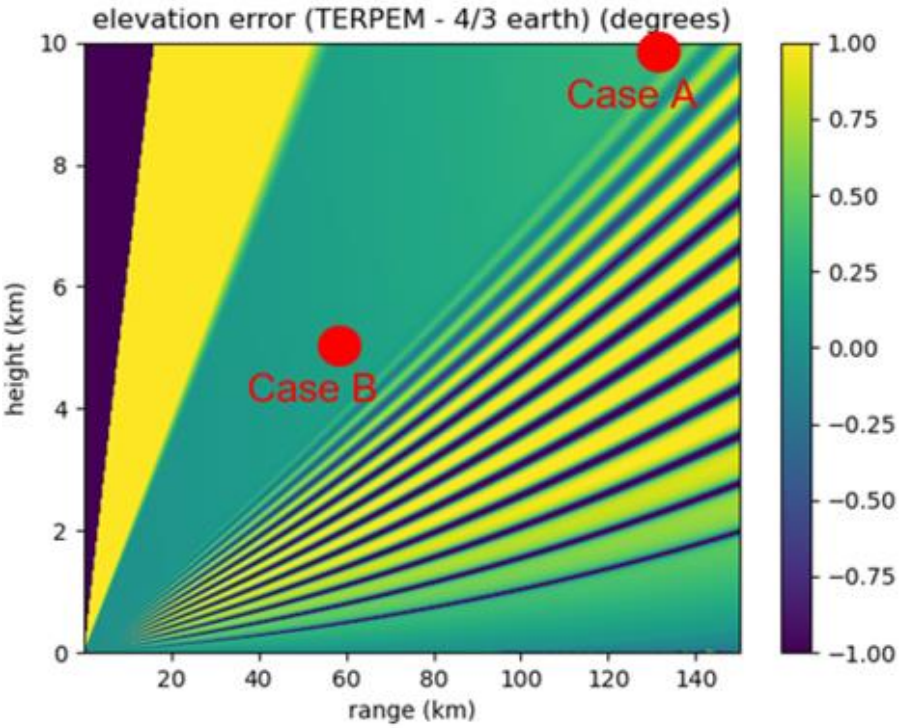

Figure 4.10 L-band radar elevation error as function of target location computed using the standard refractivity profile, with the two different positions of the cooperative target, **A** and **B**. The colour denotes the elevation error in degrees.

The elevation shows fluctuation around multipath nulls. The fluctuations are not as fine compared with the X-band radar and S-band radar due to the larger wavelength. Above the 4.5° elevation angle (the line from the origin to the upper left corner) lie no multipath fluctuations.

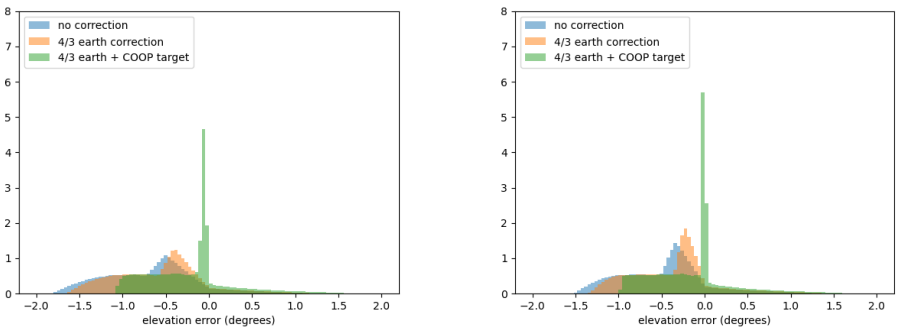

Figure 4.11 L-band radar histogram of the elevation error without correction, 4/3 Earth-radius correction and with the additional cooperative target correction with the Standard Atmosphere. On the left the histogram when the cooperative target is in position **A** and on the right the histogram when the cooperative target is in position **B**.

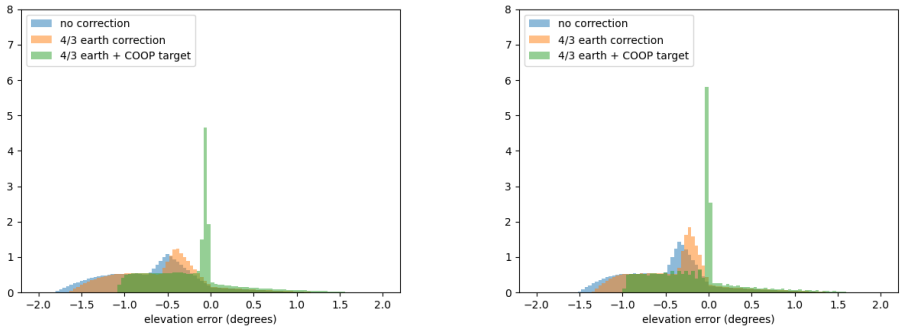

Figure 4.12 L-band radar histogram of the elevation error without correction, 4/3 Earth-radius correction and with the additional cooperative target correction using the average profile from the ITU-R P.453-11 database (North Sea). On the left the histogram when the cooperative target is in position **A** and on the right the histogram when the cooperative target is in position **B**.

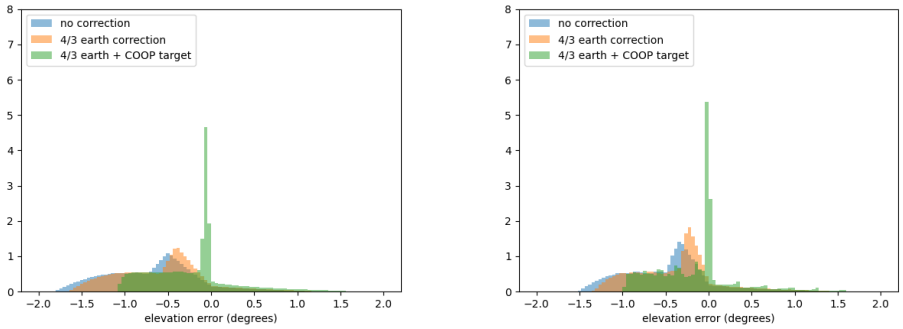

Figure 4.13 L-band radar histogram of the elevation error without correction, 4/3 Earth-radius correction and with the additional cooperative target correction with a single profile from the ITU-R P.835-6 database. On the left the histogram when the cooperative target is in position **A** and on the right the histogram when the cooperative target is in position **B**.

The histograms show the same characteristics as the X-band radar.

4.3.6.4 Results

The elevation error structure depends on the wavelength, a small wavelength (X-band) shows a fine and a large wavelength (L-band) a coarse structure. The histograms of the elevation error show that the 4/3 Earth-radius correction shifts the histogram to zero: it is a first-order correction. The cooperative target correction shifts the entire histogram to zero and narrows the histogram peak. The elevation errors are concentrated around zero. The histograms show that this correction can only be applied outside the propagation zeros with no multipath above a certain tilt elevation angle.

4.4 Multifrequency Radar Measurements

The effect of propagation depends on the radar operating frequency. Therefore, in this section, it is investigated whether radar measurements in different frequency bands can be exploited to mitigate propagation effects. For this approach a reference may not be needed.

4.4.1 Elevation Errors

In the scenarios analysis, elevation angles were estimated with the TERPEM phase estimation. This approach works well when the target is in the main beam with enough signal-to-noise ratio. Otherwise errors will be made due noise contribution is greater than the target contribution. An aspect that has not yet been discussed is the power of the pattern propagation factor. The normal refractivity profiles are compared with CARPET for a standard X-band, S-band and L-band radar. The TERPEM results are presented in the following three figures. The comparison shows that the TERPEM results lie within 2 dB of the CARPET results.

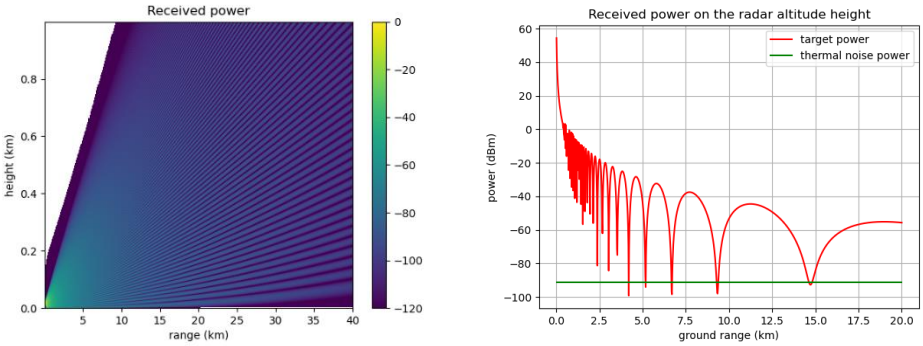

Figure 4.14 TERPEM received power in X-band with standard propagation. The antenna height and target heights are 18 m. The target has constant altitude.

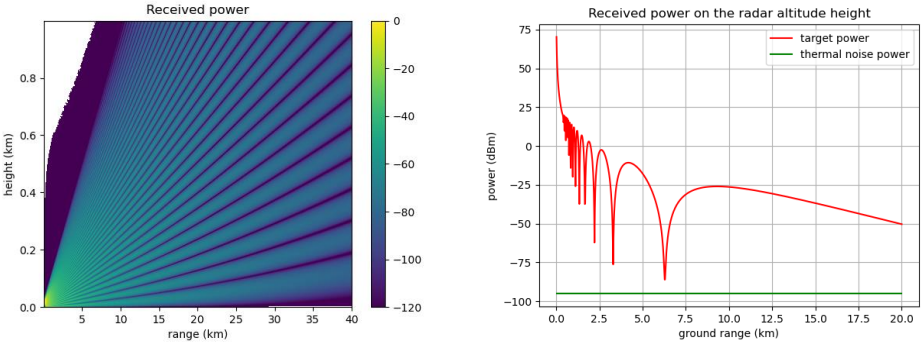

Figure 4.15 TERPEM received power in S-band with standard propagation. The antenna height and the target heights are 18 m. The target has constant altitude.

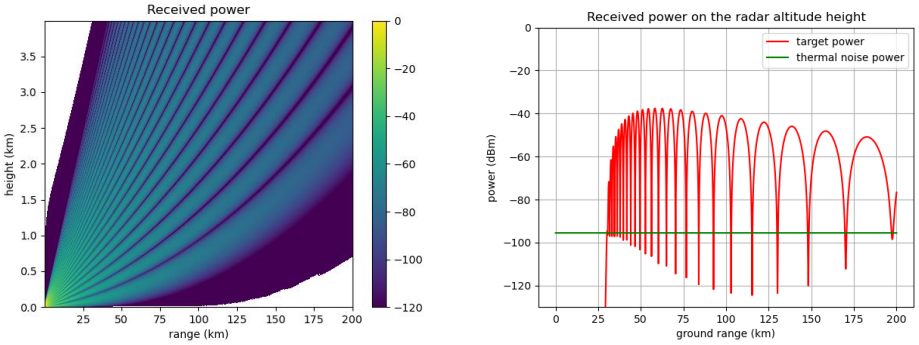

Figure 4.16 TERPEM received power in L-band with standard propagation. The antenna height and the target heights are 30 m. The target has constant altitude.

The fan beam method to estimate target elevation, as discussed in Section 0, is applied to the TERPEM propagation calculations. The characteristics of the fan beam antenna are: eleven pencil beams each with a beamwidth of 1°. An X-band radar is assumed and standard propagation. Two examples have been calculated with 50 m and 30 m antenna heights. The results are presented in Figure 4.17.

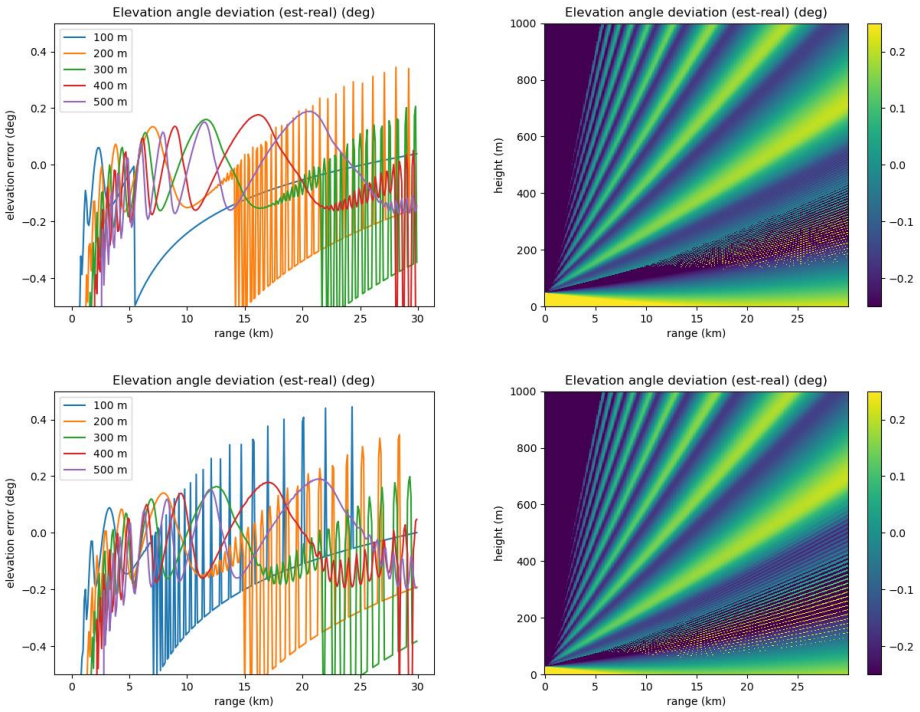

Figure 4.17 Elevation error when the fan beam method is applied for estimating the target elevation. The top shows the results for an antenna height of 50 m antenna height, the bottom row for an antenna height of 30 m. The left column shows the elevation errors for specific target heights, the right column shows the elevation error as function of range and height.

The maximum elevation error is $\frac{1}{5}\theta_e$ or 0.2° and reaches its maximum value in the middle of two fan beams. These elevation errors are relatively large. The reason is that the actual beam pattern shape was not used in the elevation estimation, it was assumed that the quadratic interpolation was sufficient. The estimated elevation fluctuates in the region with multipath effects. When successive measurements are averaged, the elevation errors will become smaller.

The fan beam method, discussed in in Section 3.1.2 works well but deserves improvement in angular estimation exploiting the actual antenna pattern.

The last part of this section presents the error histograms for the setup of the cooperative target. Figure 4.18, Figure 4.19 and Figure 4.20 present the elevation error between bands for the standard atmosphere, ITU-R P.453-11 and ITU-R P.835-6. The histogram values corresponds with the range-height values in the radar beam. Table 4.1 presents the mean and standard deviations of the radar band differences.

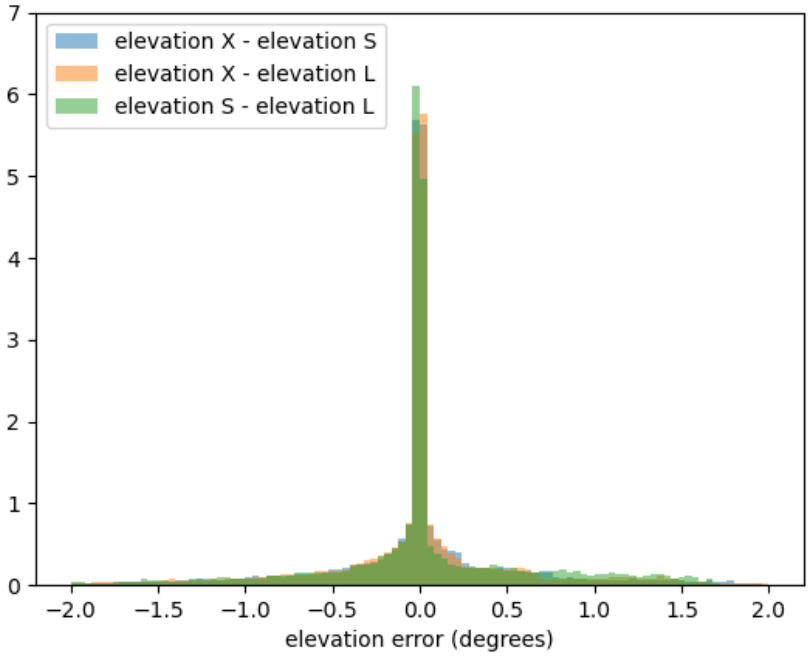

Figure 4.18 Elevation error histograms between the different bands for the standard atmosphere refractivity.

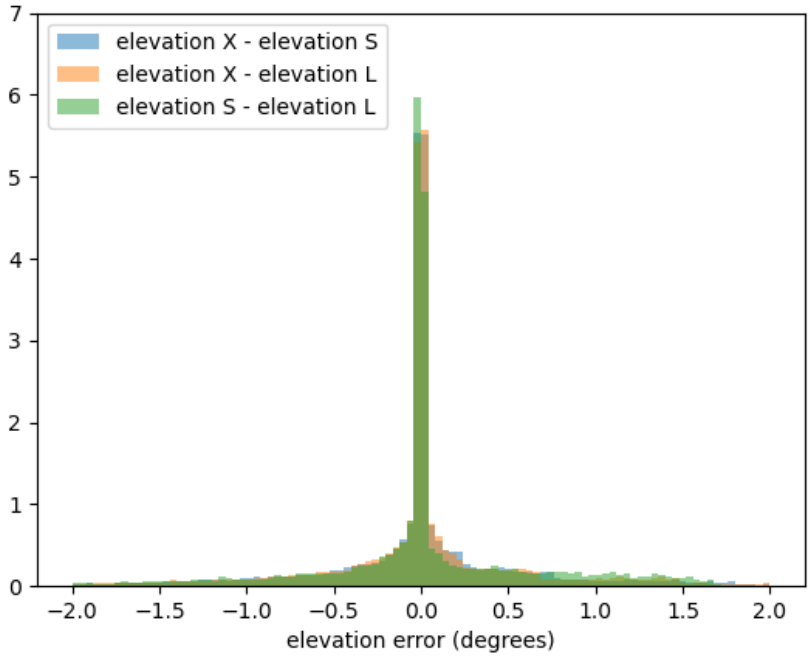

Figure 4.19 Elevation error histograms between different bands for the ITU-R P.453-11 database refractivity.

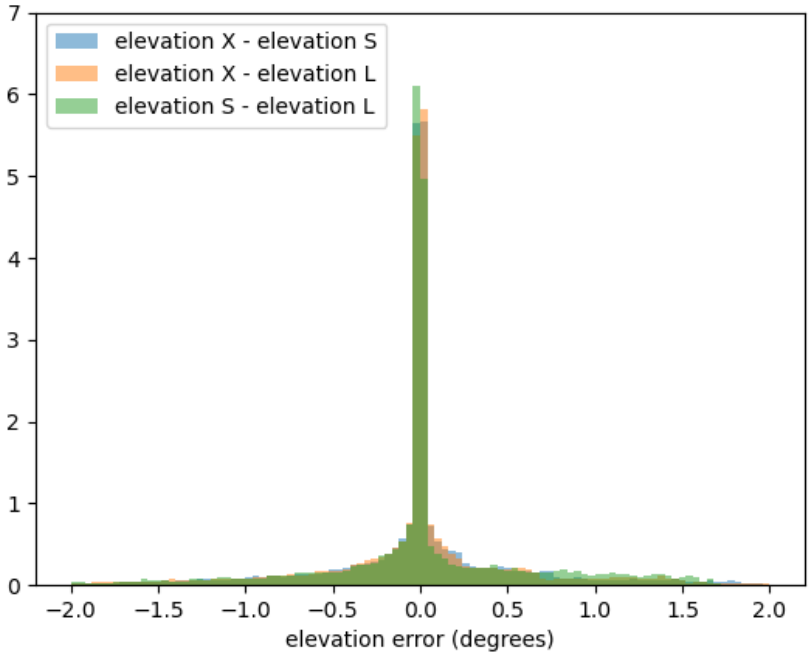

Figure 4.20 Elevation error histograms between different bands for the ITU-R P.835-6 database refractivity.

Table 4.1 Elevation errors between different bands.

Bands	Standard propagation		ITU-R P.453-11		ITU-R P.835-6	
	Mean (°)	Std (°)	Mean (°)	Std (°)	Mean (°)	Std (°)
X-band – S-band	-0.0011	0.592	0.0000	0.606	-0.0010	0.593
X-band – L-band	0.0021	0.597	0.0007	0.609	0.0020	0.597
S-band – L-band	0.0233	0.614	0.0228	0.628	0.0233	0.615

The elevation comparison show very small mean differences. The standard deviation is approximately 0.6° regardless of the areas in the beam. This is slightly higher than the 1 mrad which is often used as an acceptable error. The standard deviation is smaller in the area without multipath.

4.4.2 Range Errors

The last part of this section presents the effects of propagation on the range estimate of the target. The ray-optics method is used to provides this information. Figure 4.21 gives the overall target response where each response from that target arriving at the receiver along a different path (each with a certain electrical length) is coherently added to produce the overall response of that target. Then Figure 4.22 and Figure 4.23 present the weighted mean and the weighted standard deviation of the electrical paths lengths experienced by the individual responses comprising the overall target response in the receiver. The actual target range has been subtracted from the estimated values to display it properly. This analysis shows that the measured range fluctuates. The electrical path-length is slightly longer than the path length in free space. The differences are however small in relation to the overall target distance and may be negligible.

The results in this section show that the electrical path-length is almost equal to the geometric path-length for surface-based ducting. The differences are on the order

of a few meters and may be negligible. However, the estimated elevation angle is unstructured below the ducting height.

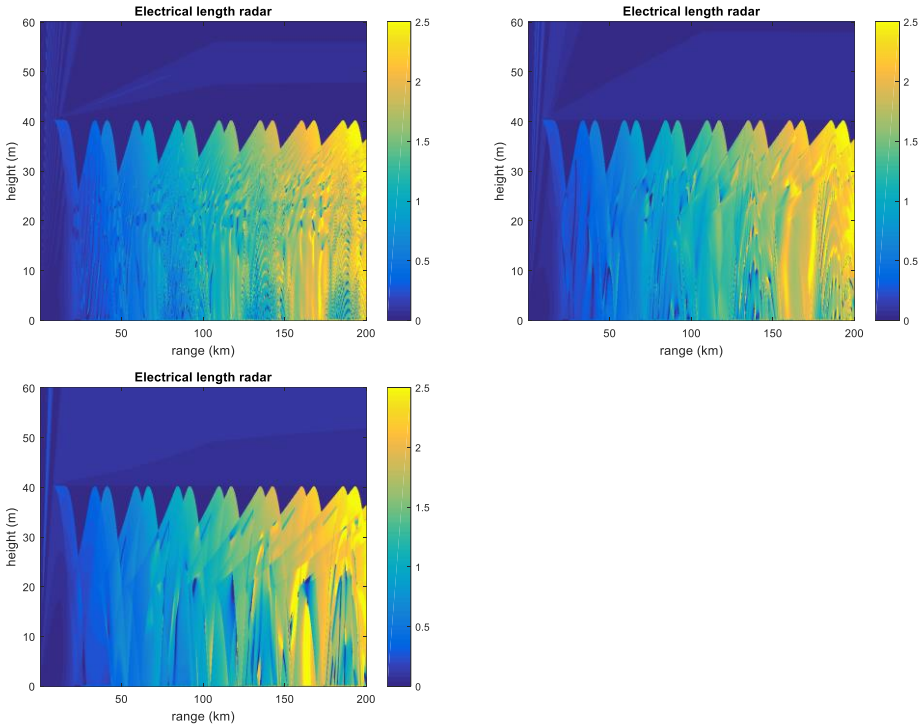

Figure 4.21 Coherent receiver addition given the electrical path length in X-band (top-left), S-band (top-right) and L-band (bottom). The values shown are the estimated value minus the grid position $\hat{L}_{electrical} - 2\sqrt{\text{height}^2 + \text{range}^2}$. The colours denote this difference in metres.

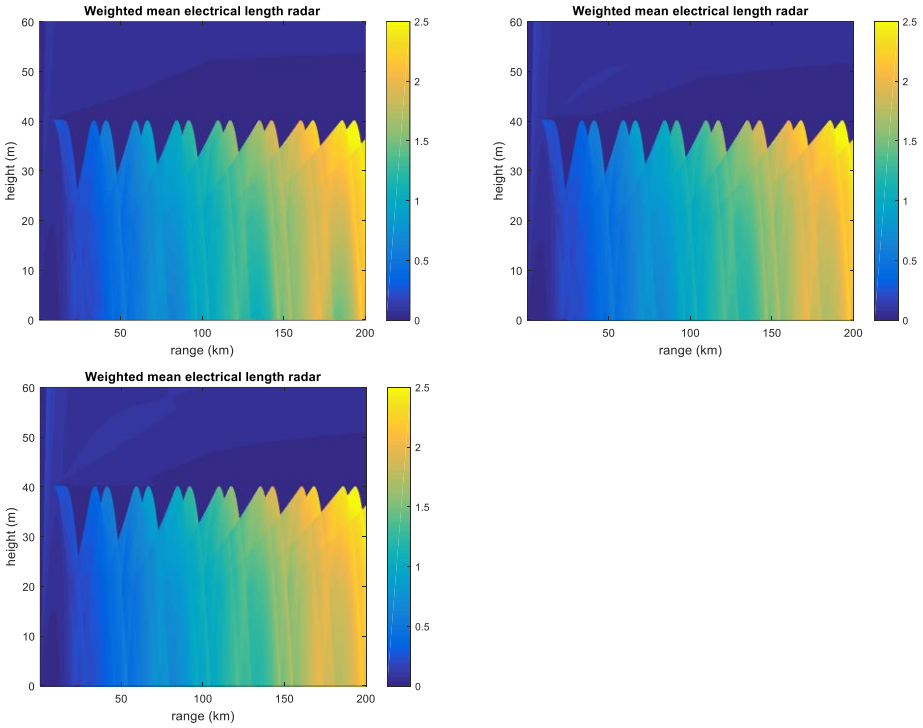

Figure 4.22 Weighted mean of the electrical path length in X-band (top-left), S-band (top-right) and L-band (bottom). The values shown are estimated value minus the grid position $\hat{L}_{electrical} - 2\sqrt{\text{height}^2 + \text{range}^2}$. The colours denote this difference in metres.

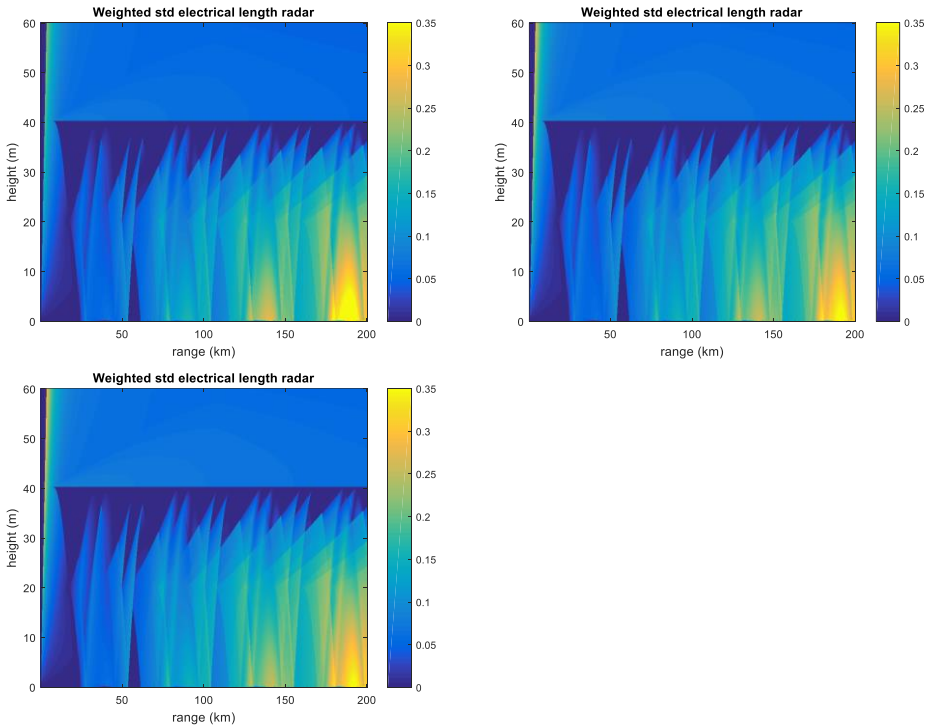

Figure 4.23 Weighted standard deviation of the electrical path length in X-band (top-left), S-band (top-right) and L-band (bottom). The colours denote the weighted standard deviation in metres.

4.4.3 Path Losses

This section describes the path losses and range error using the implemented ray-optics method, discussed in Section 3.4. When comparing losses, we need to consider the frequency in the radar equation. Suppose we have two losses L_1 and L_2 with different frequencies f_1 and f_2. The difference between the two losses is the power difference in dB

$$\Delta L = L_1(f_1) - L_2(f_2) \tag{4.4}$$

This ΔL has a constant offset which depends on the carrier frequency. To eliminate this offset, the second loss is converted to the first loss

$$\Delta L = L_1(f_1) - \left[L_2(f_2) + 20\log_{10}\left(\frac{f_1}{f_2}\right)\right] = L_1(f_1) - \left[L_2(f_2) + 20\log_{10}\left(\frac{\lambda_2}{\lambda_1}\right)\right] \tag{4.5}$$

In this way, it is possible to compare different losses belonging to different bands with each other.

A surface-based duct profile is selected because the elevation estimation is difficult in that situation. An illustration of the refractivity change over sea is presented in Figure 4.24. The following parameters are used: the radar height 20 m, duct height 40 m, duct strength (ΔM) 20 M-units, Earth radius 6370 km, refractivity index 1.00035 and reflection coefficient 0.6242. These parameters are according to the example of Zhou [26] and therefore enable a direct comparison.

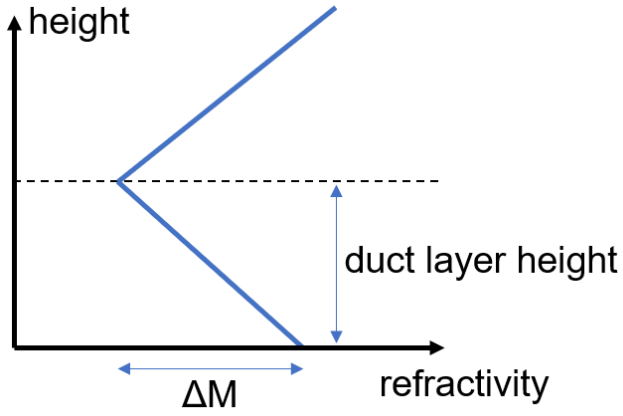

Figure 4.24 Illustration of the surface-based duct refractivity change over the sea surface.

In Figures 4.25 and 4.26, the two-way path losses are presented. The path losses fluctuate strongly in the upper ducting interval between 30 m and 40 m and at short ranges from 0 to 60 km. The path losses increase with a longer range and decrease with a lower frequency. These results are in line with the results of Zhou [26]. The figures show a discontinuity around the trapping angle. Targets below the trapping angle in the ducting area have a greater path loss than targets above the ducting height. The path losses as function of range differ for a number of reasons:

- The reflected power decreases with each reflection and this is visible in the duct area.
- The waves are pressed together increasing the electrical path-length in the radar equation. This effect is small and difficult to measure.
- The path losses in the duct area show greater variations than above the duct area due to the constructive and destructive summation in the receiver.

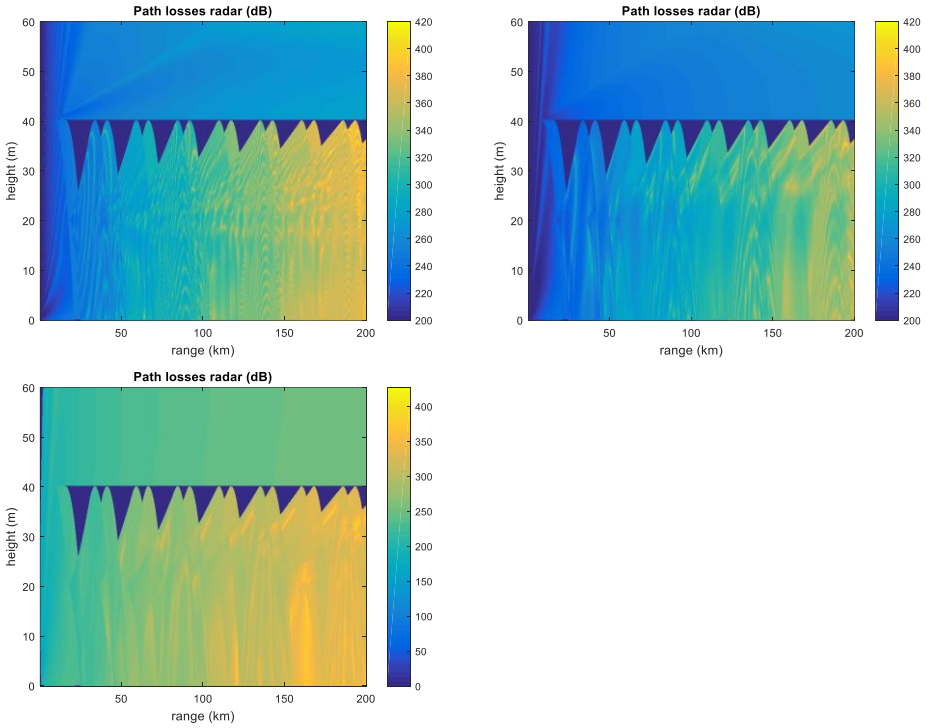

Figure 4.25 Path losses in X-band (top-left), S-band (top-right) and L-band (bottom). The colour denotes the path loss in dB.

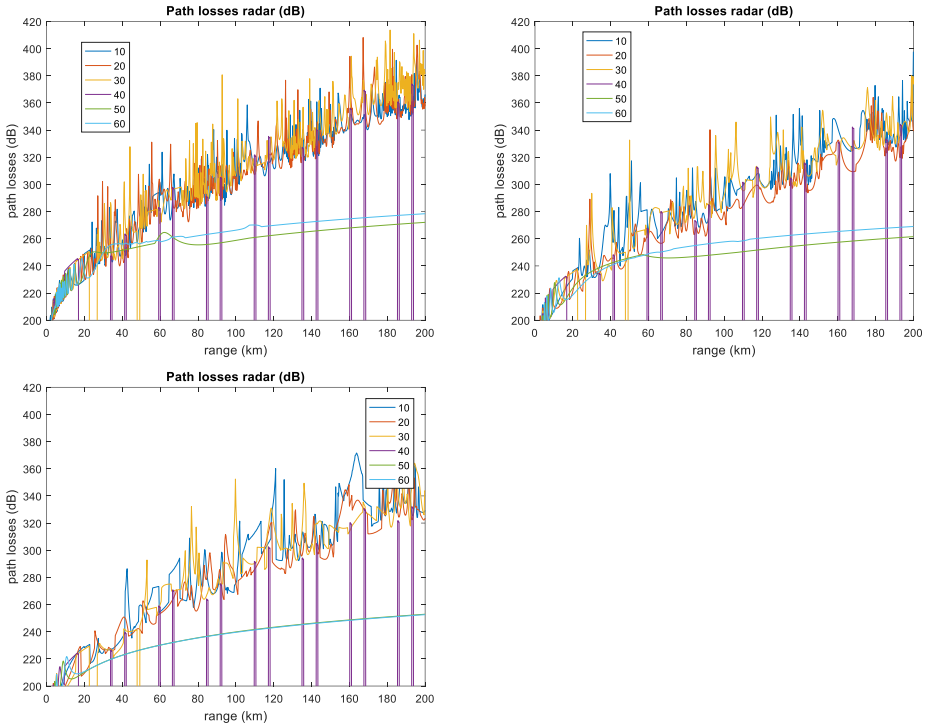

Figure 4.26 Path losses in X-band (top-left), S-band (top-right) and L-band (bottom) with a receiver height of 10, 20, 30, 40, 50 and 60 m.

The 60 m path loss corresponds to the loss differences as mentioned at the beginning of this section, this receiver height lies in the not multipath region. The other heights lie in the multipath region and comparison is difficult.

Figure 4.27 shows the observed target elevation. The elevation at which a target is observed, appears unstructured if the target is below the ducting height. Above the ducting height, the elevation at which a target is observed is in accordance with the target position.

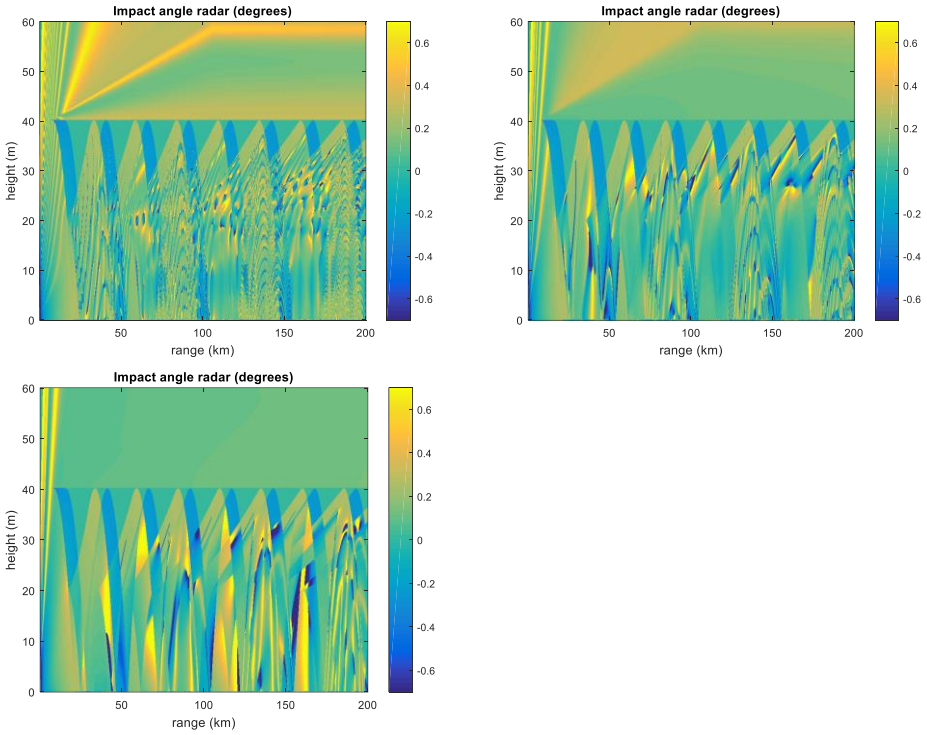

Figure 4.27 Receiver angle in X-band (top-left), S-band (top-right) and L-band (bottom). The colour denotes the estimated elevation angle in degrees.

4.4.4 Discussion

In this section the X-band, S-band and L-band radars are compared with each other. The elevation angles, range estimates and losses have been compared. The results show that the results differ for the region with multipath, the region without multipath and the region below the duct height. The multipath region and the non-multipath region is bounded by a certain elevation angle below which multipath is present and above without multipath. The separation elevation angle is the same for all bands. This means that multipath appears in the same region for all bands. The tarping duct appears below the duct height.

The elevation differences between the three bands are small, almost equivalent, in the region without multipath. Larger elevation differences arise in the area with multipath and below the duct height. These differences depend on where the constructive and destructive interference effects lie in the individual bands.

The results obtained with the ray-optics show that the electrical path-length is almost equal to the geometric path-length for surface-based ducting.
The differences are on the order of a few meters and may be negligible in the multipath region. However, the estimated elevation angle is unstructured below the ducting height.

The loss comparison shows that the losses in the region without multipath can be related to each other after frequency correction. In this region the loss differences between different bands are small after frequency correction. The correction follows from the radar formula. In the area with multipath, the loss differences are irregular. In this multipath region we are dealing with the frequency correction, but also constructive and destructive interference due to multipath. It is difficult to relate the

constructive and destructive regions in the different frequency bands and frequency agility with elevation null filling does not work.

5 Conclusion

The range and angle to a target as measured by radar depend on the atmospheric propagation conditions and on the radar characteristics. Therefore, measurements of the same target, acquired by radar systems operating in different frequency bands or by radar systems in different positions, may be inconsistent due to diverse propagation effects. If disregarded, such measurement inconsistencies complicate the fusion of the radar observations. By predicting the propagation effects and correcting the radar measurements for these effects, inconsistences can be mitigated allowing fusion of the observations.

Atmospheric propagation effects can be predicted using propagation models. However, the accuracy of this prediction depends on the spatial and temporal resolution and on the accuracy of the atmospheric data used to run the model. The means to gather accurate atmospheric data on board a platform on open sea are very limited, such that in turn the accuracy of the predictions of radar wave propagation is limited. Therefore, within this project it was investigated whether information on the current observation errors due to propagation effects can be extracted from the radar measurements themselves. It was furthermore investigated whether this information can be applied to correct the radar measurements, without the need to determine the full refractivity profile of the atmosphere. Within the project, two approaches were investigated.

For the first approach it is assumed that single-band radar measurements are available. To be able to exploit single-band measurements for the assessment and correction of propagation effects, a reference is needed. Such a reference could be steady clutter or a ‘cooperative’ target with known position such as an airliner sending ADS-B messages. It was investigated whether the elevation error estimated based on the known position of a cooperative target, can be applied to correct the measured elevation of targets in other positions as well. The applied method is expandable with multiple cooperative targets and other calibration targets such as satellites. The investigation showed that this approach is indeed feasible in regions without multipath. The applied method is applicable in multipath areas, but areas of constrictive and destructive interference should be taken into account. By applying frequency agility in combination with elevation filling, the destructive interference areas are filled. The destructive interference areas then move as a function of the frequency. In the constructive interference areas, the method with cooperative goals can also be applied. However, the effectiveness depends highly on the actual measurement geometry and atmospheric conditions and it is therefore difficult to draw general conclusions.

In the second approach multiband radar measurements are exploited. Combining radar measurements in different frequency bands, helps to mitigate propagation effects, because these effects are frequency-dependent. This approach circumvents the need for a reference but not all problems can be solved.
The elevation widths of the destructive regions in a single band become smaller as the frequency increases. Applying different bands reduces the destructive areas. Frequency agility in combination with ‘elevation filling’ is applied to fill the remaining destructive areas. The area below the ducting height remains a difficult area even with multiple frequency bands. The main problem is a reliable elevation estimator.

Since the elevation widths of the destructive regions in a single band become smaller as the frequency increases, averaging many successive measurements with different frequencies could provide a solution for a reliable elevation estimate. Even if the refractivity profile is known, a correction below the duct height is difficult. Again it is difficult to draw general conclusions because the overall effect depends on the measurement geometry and the actual atmospheric circumstances.
In general it is likely that awareness of the current propagation conditions improves the data combination process, since it can be predicted to some extent when measurements (in a certain frequency band) degrade due to propagation effects.

Awareness of the actual radar wave propagation conditions is important since propagation effects can have a significant impact on radar measurements and overall performance. In this study it has been shown that information about the current propagation conditions and the related measurement errors can be extracted from the radar measurements themselves. Taking into account atmospheric propagation effects and correcting for them, will become more relevant in view of future (multiplatform) networked operations and long-range applications such as ballistic missile defence and space situation awareness. The tools implemented within the current project can be used for performance evaluations in other projects, such as “Concepts for Networked Operation” currently running within the framework of the Radar Programme V1908.

6 References

[1] A.K. Shukla, D.J. Fraser, A. Lockton et al., “The impact of tropospheric propagation on data fusion from multiple radars,” Proc. FUSION, Philadelphia, U.S.A., June 27 – July 1, 2005.

[2] J. Derksen, “Radar performance modelling. A study of radar performance assessment accuracy sensitivity to the resolution of atmospheric input data. Case studies of North Sea environments,” MSc Thesis, Delft University of Technology, 2016.

[3] E.R. Bruin, “On propagation effects in maritime situation awareness,” MSc Thesis, Utrecht University, 2016.

[4] R. Russell, UCAR Center for Science Education. Available online: https://scied.ucar.edu/learning-zone/atmosphere/layers-earths-atmosphere [visited November 19, 2021].

[5] J.P. Skura, Worldwide anomalous refraction and its effects on electromagnetic wave propagation, Johns Hopkins APL Technical Digest, vol. 8, no. 4, pp. 418-425, 1987.

[6] A.W. Doerry, “Earth curvature and atmospheric refraction effects on radar signal propagation,” Sandia Report, SAND2012-10690, January 2013. Available online: https://www.researchgate.net/publication/277011644_Earth_Curvature_and_Atmospheric_Refraction_Effects_on_Radar_Signal_Propagation [visited December 1, 2021].

[7] A.W. Doerry, “Correcting radar range measurements for atmospheric propagation effects,” SPIE 2014 Defense Security Symposium, 2014.

[8] B.M. Fannin and K.H. Jehn, “A study of radar elevation-angle errors due to atmospheric refraction,” IRE Trans, Antennas and Propagation, vol. 5, no. 1, pp. 71-77, 1957.

[9] W.B. Sweezy and B.R. Bean, “Correction of atmospheric refraction errors in radio height finding,” National Bureau of Standards, Journal of Research, vol. 67D, no. 2, pp. 139-151, 1963.

[10] P.E. Schmid, “Atmospheric tracking errors at S-band and C-band frequencies,” Tech. Rep. NASA TN D-3470, NASA, 1966.

[11] “Atmospheric refraction measurements and related efforts,” Tech. Rep., Range Commanders Council, Electronic Trajectory Measurements Group, 1979.

[12] “Survey of radar refraction error corrections,” Tech. Rep. RCC 266-16, Range Commanders Council, Electronic Trajectory Measurements Group, 2016.

[13] E.H. Burgess and K.L. Horgan, “Applying Numerical Weather Prediction data to enhance propagation prediction capabilities to improve radar performance prediction,” Proc. NATO SET-244 Symposium, Den Helder, The Netherlands, October 31 – November 2, 2017.

[14] A.G. Huizing and A. Theil, “CARPET Version 3 user manual,” TNO, June 2021. Available online: https://www.tno.nl/media/11470/carpet3manual.pdf [visited December 22, 2021].

[15] W.L. Patterson, C.P. Hattan, H.V. Hitney, R.A. Paulus, A.E. Barrios, G.E. Lindem and K.D. Anderson, “Engineer's Refractive Effect s Predistion System (EREPS) Revision 2.0”, Naval Ocean System Center, 1990.

[16] http://www.signalscience.com/index.html [visited December 22, 2021].

[17] E. Heemskerk, “RF propagation measurement and model validation during RF/IR synergy trial VAMPIRA,” Proc. SPIE, vol. 5981, 2005.

[18] A. Theil, R.G. Tan, J.J. Boschma and S. Jacobs, “Model-aided feature extraction,” Proc. NATO SET-244 Symposium, Den Helder, The Netherlands, October 31 – November 2, 2017.
[19] A. Theil, “What TERPEM calculates”, TNO, 2010.
[20] O. Ozgun, M. Kuzuoglu, G. Apaydin and L. Sevgi, “PETOOL: MATLAB-based one-way and two-way split-step parabolic equation tool for radiowave propagation over variable terrain,” Computer Physics Communications, vol. 182, no. 12, pp. 2638-2654, 2011.
[21] O. Ozgun, V. Sahin, M.E. Erguden, G. Apaydin, A.E. Yilmaz, M. Kuzuoglu and L. Sevgi, “PETOOL v2.0: Parabolic Equation Toolbox with evaporation duct models and real environment data”, Computer Physics Communications, vol. 256, 2020.
[22] R.A. Sprague and P. Babu, “A new propagation prediction tool for earth-space geometries for the advanced refractive effects prediction system (AREPS),” Proc. IEEE MILCOM, San Diego, U.S.A., November 16-19, 2008.
[23] C. Yin, “Comments on PETOOL”, Hefei Electronics Engineering Institute, 2021.
[24] J.A. Caicedo, “Propagation in Evaporation ducts with applications to detecting sea-surface targets using MIMO radar Systems”, master thesis, University of Florida, 2011.
[25] E. Dinc and O.B. Akan, “Channel Model for the Surface Ducts: Large-Scale Path-Loss, Delay Spread, and AOA”, IEEE Transactions on Antennas and Propagation, volume 63, no. 6, June 2015.
[26] H. Zhou, J. Wang, Q. Sun, W. Feng, L. You and C. Yu, “A Ray-Optics Approach for Evaporation Duct Channel Modelling”, IEEE, 2018.
[27] W. Wang, R. Raulefs and T.Jost, “Fading characteristics of maritime propagation channel for beyond geometrical horizon communications in C-band”, Springer CEAS Space Journal, 2019.
[28] B.R. Mahafza, “Radar System Analysis and Design using Matlab, third edition”, CRC Press, 2013.
[29] J.D. Parsons, “The Mobile Radio Propagation Channel”, John Wiley & Sons, 2000.
[30] H. Godrich, A.M. Haimovich and R.S. Blum, “Target Localization Accuracy Gain in MIMO Radar-Based Systems”, IEEE Transactions on Information Theory, 2010.
[31] R.J. de Jong, M.P.G. Otten, J.J.M. de Wit and D.A. Boersma, “System concepts for a reconfigurable LSX-band radar suite,” TNO, Tech. Rep. TNO 2020 R11828, 2021.
[32] “Reference standard atmospheres,” Recommendation ITU-R P.835-6, ITU-R, 2017.
[33] “Reference standard atmospheres Datasets,” Recommendation ITU-R P.835-6, ITU-R, 2017. Available online: https://www.itu.int/rec/R-REC-P.835-6-201712-I/en [visited December 22, 2021].
[34] J.H. Richter, “Sensing of radio refractivity and aerosol extinction,” Proc. IEEE IGARSS, Pasadena, U.S.A., August 8-12, 1994.
[35] A. Karimian, C. Yardim, P. Gerstoft et al., “Refractivity estimation from clutter: An invited review,” Radio Sci., vol. 46, 2011.
[36] C. Yardim, P. Gerstoft and W.S. Hodgkiss, “Estimation of radio refractivity from radar clutter using Bayesian Monte Carlo analysis,” IEEE Trans. Antennas Propag., vol. 54, no. 4, pp. 1318-1327, April 2006.

[37] C. Yardim, P. Gerstoft and W.S. Hodgkiss, “Tracking refractivity from clutter using Kalman and particle filters,” IEEE Trans. Antennas Propag., vol. 56, no. 4, pp. 1058-1070, April 2008.
[38] B. Leng Cheong, R.D. Palmer, C.D. Curtis et al., “Refractivity retrieval using the phased-array radar: First results and potential for multimission operation,” IEEE Trans. Geosci. Remote Sensing, vol. 46, no. 9, pp. 2527-2537, September 2008.
[39] C. Lafleur, “Spacecraft encyclopedia Radar calibration satellites,” website. Available online: http://claudelafleur.qc.ca/Scfam-radarcalibration.html [visited December 22, 2021].
[40] “Live real time satellite tracking and predictions,” website. Available online: https://www.n2yo.com/satellites/?c=31 [visited December 22, 2021].
[41] H. Lee, T. Lee, J. Chun and J. Lee, “Target positioning with surveillance radar by the estimation of the atmospheric refractivity profile,” IEEE Trans. AES, vol. 56, no. 3, pp. 2245-2255, June 2020.
[42] S. Fortunati, F. Gini, M.S. Greco et al., “Correction of refracted propagation effects for airborne radar tracking,” IEEE Trans. AES, vol. 49, no. 1, pp. 20-41, January 2013.
[43] S. Katsougiannopoulos, C. Pikridas, D. Rossikopoulos et al., “Tropospheric refraction estimation using various models, radiosonde measurements and permanent GPS data,” Proc. FIG XXIII Congress & XXIX General Assembly, Munich, Germany, October 8-13, 2006.
[44] O. Jicha, P. Pechac, V. Kvicera and M. Grabner, “Estimation of the radio refractivity gradient from diffraction loss measurements,” IEEE Trans. Geosci. [45Remote Sensing, vol. 51, no. 1, pp. 12-18, January 2013.]
[46] International Telecommunication Union, “Recommendation ITU-R P.1144-10 (02/2019), Guide to the application of the propagation methods of Radiocommunication Study Group 3”, 2019.
[47] D.K. Barton, “Radar Equations for Modern radar”, 2013.
[48] M.I. Skolnik, “Radar Handbook, Third Edition”, 2008.
[49] A.E. Barrios, W.L. Patterson, and R.A. Sprague, “Advanced Propagation Model (APM) Version 2.1.04 Computer Software Configuration Item (CSCI) Documents”, 2007.

A Long-Term Averaged Atmospheric Data

Over years atmospheric measurements have been measured and analysed. These long atmospheric measurements yield average refractivity profiles. One example of an extended database of long-term atmospheric profiles is the database provided by the International Telecommunication Union (ITU) related to the Recommendation ITU-R P.835-6 [32]. This database includes monthly averages of vertical profiles of temperature, pressure and relative humidity for 353 locations spread over the world. This database is freely available [33].

In the propagation models, long-term average refractive profiles might be used instead of the Standard Atmosphere. However, for accurate radar performance prediction, the atmospheric data should be updated every two to four hours and in turbulent conditions even more often. Consequently, using long-term average refractivity profiles will not suffice for accurate radar performance prediction in the more fluctuating lower-air layer.

The average profiles are based on ten years of radiosonde measurements. The vertical profiles cover 0 km to 16 km altitude. The altitude step depends on the structure of the profile. In the recommendation, reference profiles are provided to extrapolate the profile for altitudes above 16 km.

Average profiles of these 353 locations were calculated on a latitude and longitude grid over the entire earth. The average profiles each have their own altitude spacing derived from the variations of the vertical profiles. The altitude spacing is chosen in such a way that altitude interpolation is possible while preserving information. The database gives the average temperature, pressure and relative humidity for each month and at four times of the day: 0, 6, 12 and 18 hours. So the total number of profiles for each location is 48. Linear Interpolation in place and time is described by the ITU standard [46]. The figures below show the ground pressure, ground temperature and ground vapour density available in the ITU-R P.835-6 database for midnight during August.

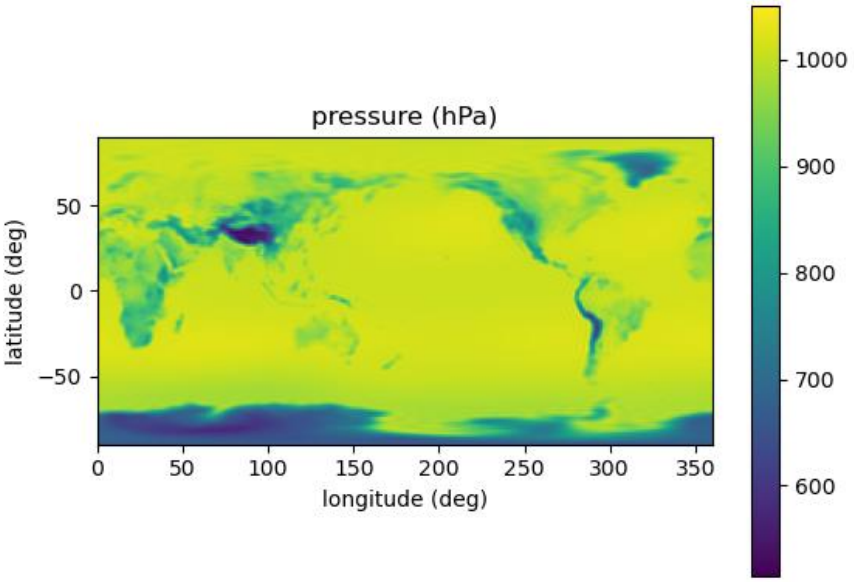

Figure A.1 Ground pressure from the ITU-R P.835-6 database (August, midnight).

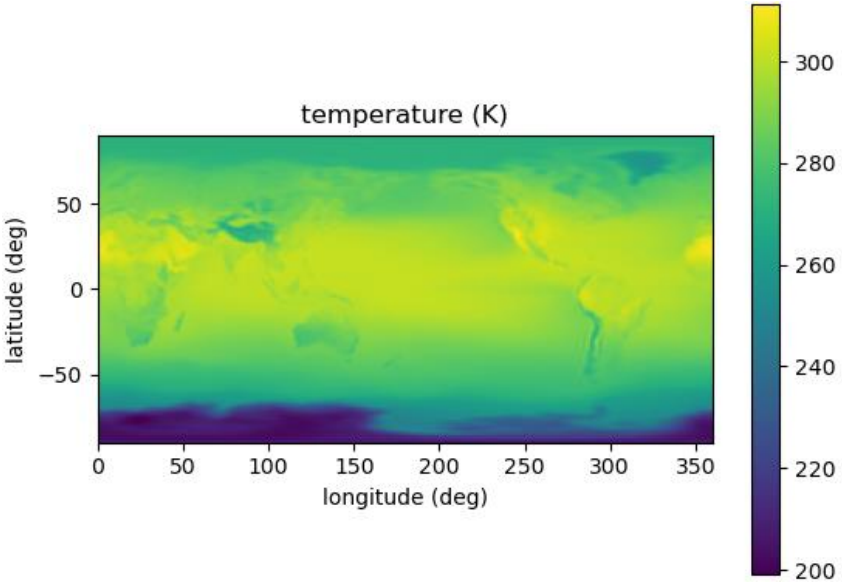

Figure A.2 Ground temperature from the ITU-R P.835-6 database (August, midnight).

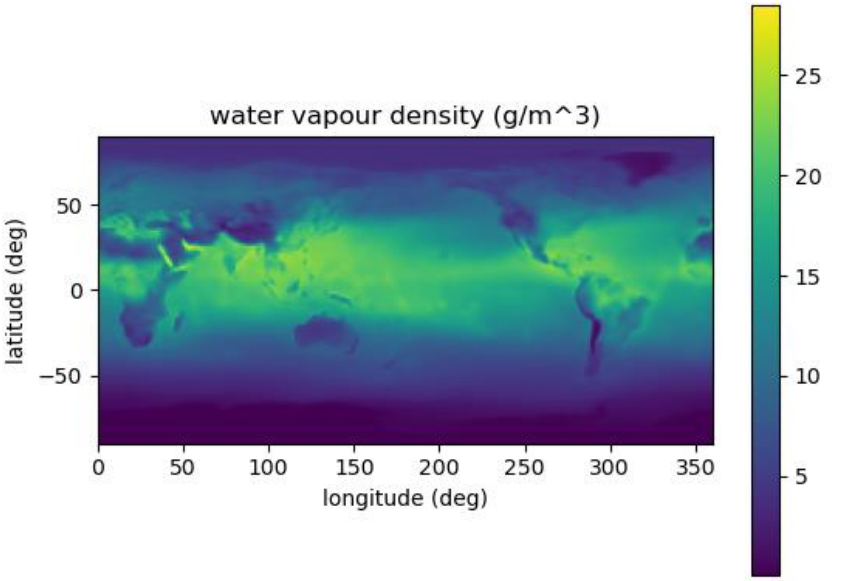

Figure A.3 Water vapour density from the ITU-R P.835-6 database (August, midnight).

A.1 Long Term Elevation Estimates

In this section long-term average refractivity profiles are applied to estimate elevation corrections. The cases discussed in this section, the complex propagation factors and associated elevation angles are calculated with TERPEM, assuming a monostatic L-band radar on the North Sea. In Figure A.4 the elevation error is shown as function of target position for one example of a refractivity profile taken from the ITU-R P.835-6 database (North Sea). The elevation estimate of targets with low elevation are consistently overestimated. These errors are smaller than with a multipath zero. Outside the multipath zeros, the elevation can be reliably estimated with a mono pulse-like measurement.

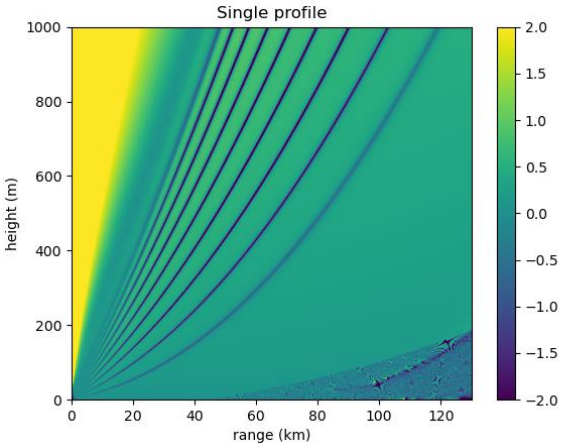

Figure A.4 Elevation error as function of target position for a single refractivity profile taken from the ITU-R P.835-6 database (North Sea). The colour denotes the elevation error in degrees. The elevation error is bounded between -2° and +2°.

To gain insight in the behaviour of the elevation error as function of the refractivity profile, the average elevation error over all 48 refractivity profiles in the ITU-R P.835-6 database (for the North Sea) has also been determined, see Figure A.5. Comparing the two figures we see that the coordinates of the multipath zeros occur around the same positions, the average elevation progresses to the right. The average elevation error does not deviate much from the elevation error as determined for a single refractivity profile shown in Figure A.4. This conclusion applies to this North-Sea scenario.

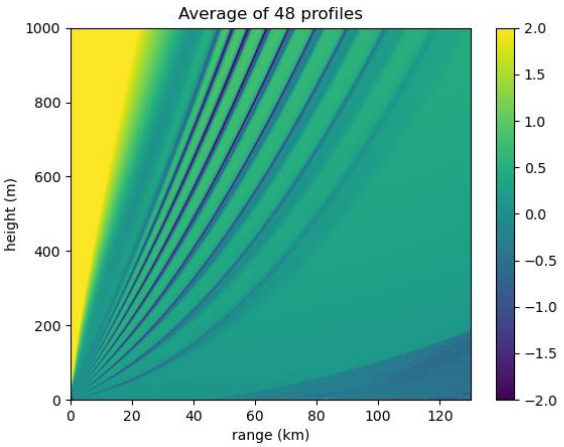

Figure A.5 Average elevation error as function of target position over all 48 refractivity profiles taken from the ITU-R P.835-6 database (North Sea). The colour denotes the elevation error in degrees.

A.2 Long Term Elevation Histograms

The long term elevation histogram analysis uses the 48 refractivity profile as available in the ITU-R P.835-6 database for the North Sea, the standard propagation profile and the geodetic reference, and the geodetic reference corrected for 4/3 Earth-radius propagation, see Figure A.6. Different statistical properties can be calculated for each range-altitude cell. This is circumvented by looking at histograms. Four different histograms are shown in Figure A.7.
The histograms for each cell are combined into a single histogram for the entire range-height grid. This is possible because the histograms are calculated relative to a reference grid. The reference is the geodetic solution with elevation angle or the standard propagation solution.

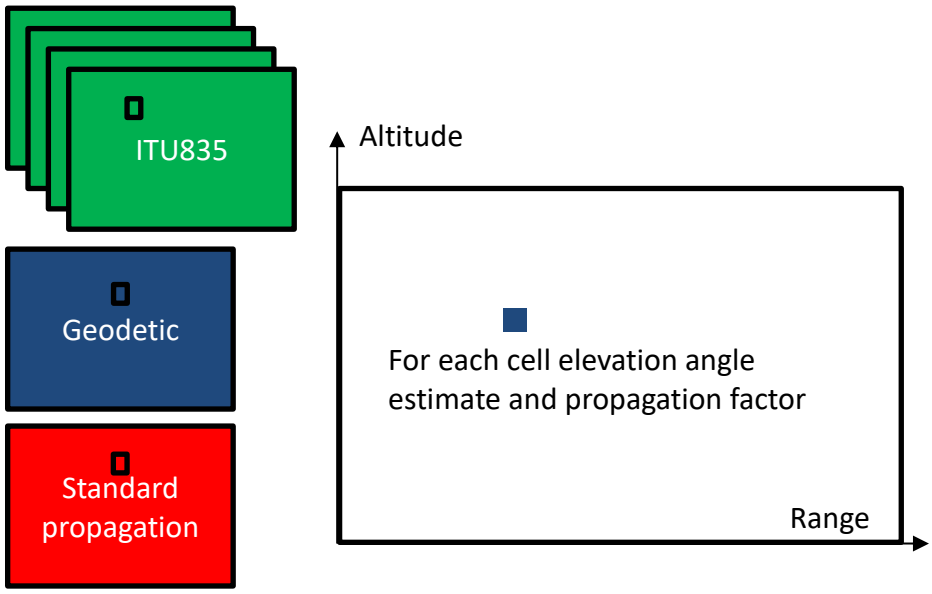

Figure A.6 Long-term scenario. In green the 48 refractivity profiles from the ITU-R P.835-6 database with elevation angles and propagation factors, in red the standard propagation pattern elevation angles and propagation factors and in blue the geodetic reference elevation.

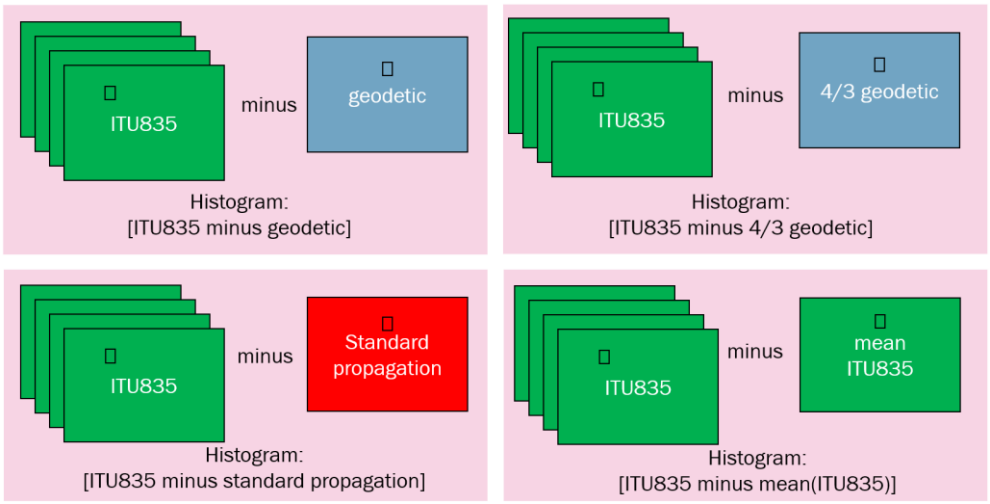

Figure A.7 Calculated approach. The square is a selected range-height cell with corresponding histogram.

The following, notations have been used to describe the histograms. A single geodetic elevation estimate for each (k_r, k_h) grid point is indicated as $\theta^{geo}_{k_r,k_h}$ where the subscript indicates the grid and the superscript the elevation type. The geodetic elevation corrected for the 4/3 Earth-radius propagation is $\theta^{geo,\frac{4}{3}earth}_{k_r,k_h}$. The elevation obtained with TERPEM with the standard refractivity profile is symbolised as $\theta^{standard}_{k_r,k_h}$. The elevation calculated using the profiles from the ITU-R P.835-6 database has an additional "(m,h)" index in the superscript to indicated the month and day; $\theta^{ITU835,m,h}_{k_r,k_h}$, where $m = 1,2 \ldots 12$ and $h = 0,6,12,18$ hour. The related mean hourly value of the elevation is symbolised as $\theta^{ITU835,h}_{k_r,k_h}$. The observations, o ,or histogram inputs are

$$\begin{aligned} o^{m,h}_{k_r,k_h} &= \theta^{ITU835,m,h}_{k_r,k_h} - \theta^{geo}_{k_r,k_h}, \\ o^{m,h}_{k_r,k_h} &= \theta^{ITU835,m,h}_{k_r,k_h} - \theta^{geo,\frac{4}{3}earth}_{k_r,k_h}, \\ o^{m,h}_{k_r,k_h} &= \theta^{ITU835,m,h}_{k_r,k_h} - \theta^{standard}_{k_r,k_h}, \\ o^{m,h}_{k_r,k_h} &= \theta^{ITU835,m,h}_{k_r,k_h} - \theta^{ITU835,h}_{k_r,k_h}. \end{aligned} \quad \text{(A.1)}$$

Intermediate results of the histogram calculations are shown in Figure A.8 and Figure A.9. The figures show the difference values of a single profile from the ITU-R P.835-6 database with the geodetic reference profile and the average of the 48 profiles for the North Sea from the ITU-R P.835-6 database. Both figures indicate large errors in the multipath regions. The single profile/geodetic difference (Figure A.8) exhibits large error in the area outside the beam, the area in the left upper corner and in the area in the lower right corner, where there is no line-of-sight. These areas are smoothed in the difference between the single profiles and the averaged profile (Figure A.9).

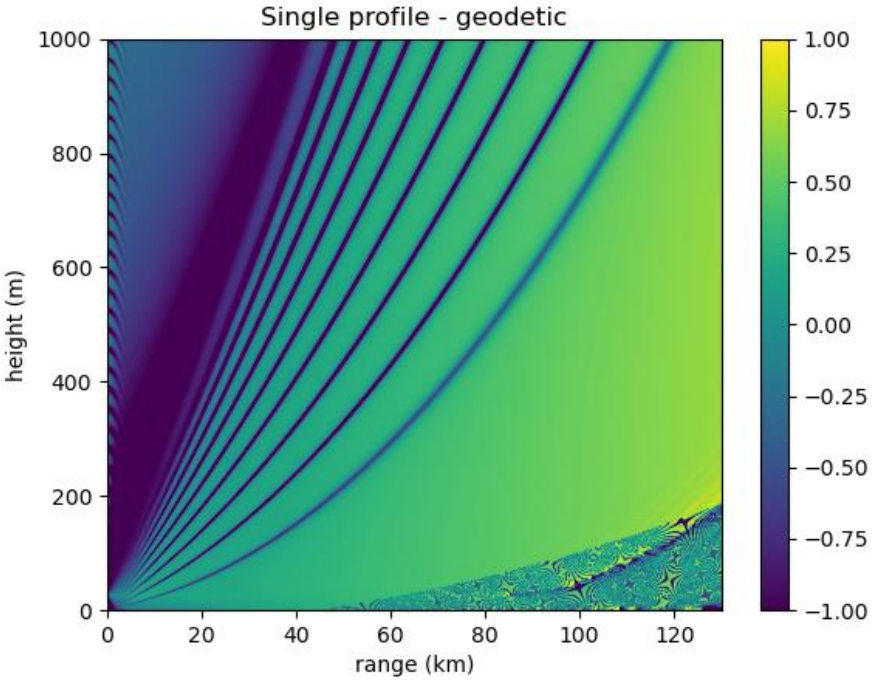

Figure A.8 Difference between the elevation computed using a single profile from the ITU-R P.835-6 database (North Sea) and the geodetic reference. The colour denotes the elevation in degrees.

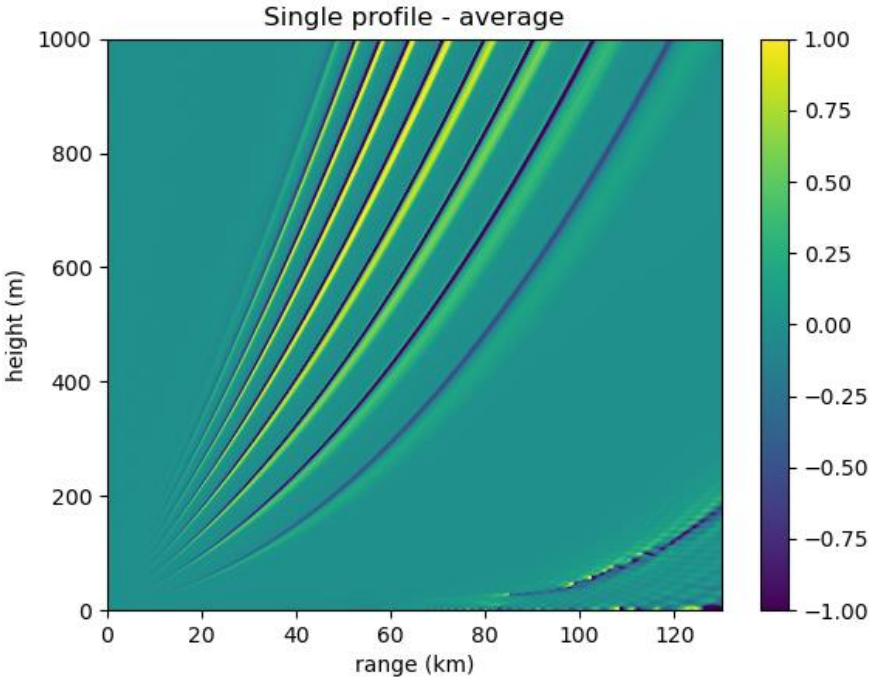

Figure A.9 Difference between the elevation computed using a single profile and using the averaged profile from the ITU-R P.835-6 database. The colour bar is in degrees.

Two different histograms are composed. The first histogram uses all elevation angles, see Figure A.10. This histogram includes the elevation estimates with a large error in places where little energy is received due to propagation effects.

The second histogram in Figure A.11 shows the results if the maximum absolute elevation error is limited to 1°.

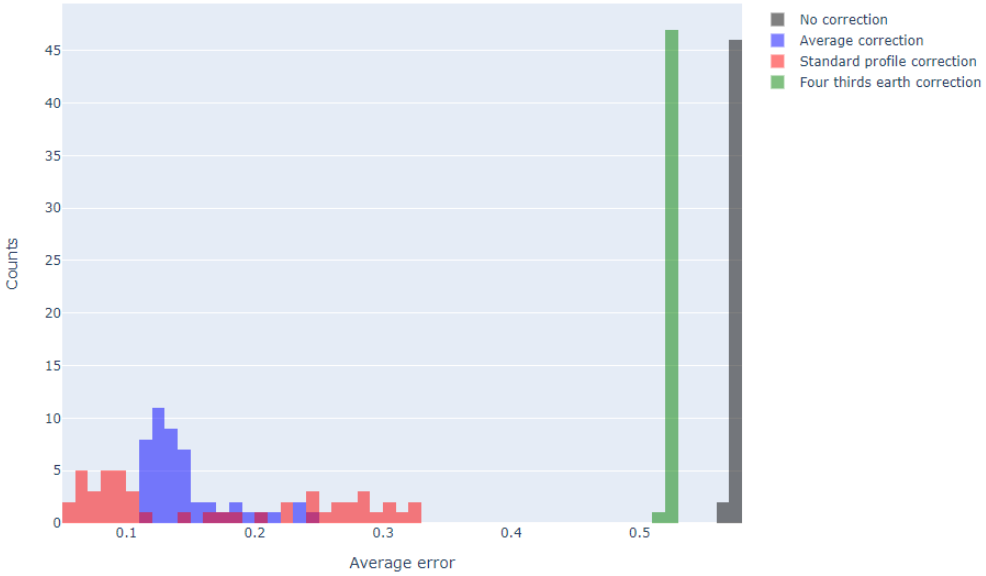

Figure A.10 Histogram of absolute elevation errors over the entire range-height grid. The horizontal axis is the absolute value of the elevation error in degrees.

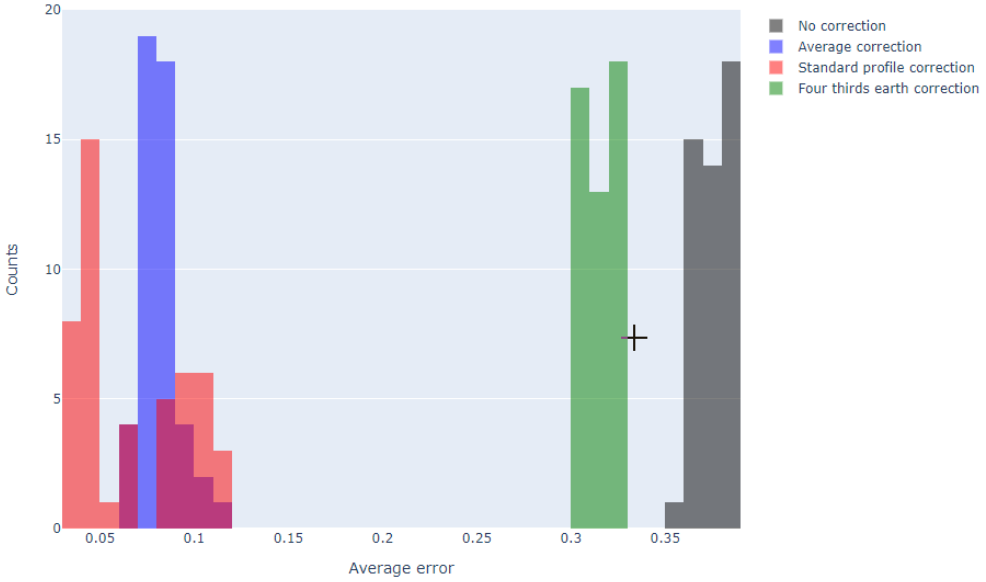

Figure A.11 Histogram of absolute elevation errors over the range-height grid with the exception of absolute elevation errors greater than 1°. The horizontal axis is the absolute value of the elevation error in degrees.

The histograms of this North-Sea scenario show that:

- The elevation errors when propagation influences are not taken into account with geodetic or 4/3 geodetic references are larger than when propagation influences are taken into account. This is understandable because the more propagation effects are accounted for, the better the estimate is.
- The histogram for standard propagation profile is staggered. A global correction has been applied. The histogram of the elevation computed from the average profile is peaked and lies around a central value. This suggests that there is an offset error. On average, the errors are similar.

In summary, it can be said that the more information about the refractivity profile is used in the elevation estimation and correction, the smaller the error.
In practice, however, obtaining information about the atmosphere is the bottleneck (as explained in Section 4.2).

Distribution list

Report & Managementuittreksel TNO 2022 R10073 (V1908)

Ten behoeve van de distributie binnen Defensie

Dynamisch Informatie Beheer, Bestuursstaf (DIB-BS) *MPC 58B*	*cd*

DEFENSIE

DGB/DOBP/S&T Kol M. de Rivecourt MSc (Ministerie van Defensie)	pdf
DGB/DOBP/S&T–P&P Defensie Programma procesbegeleider D.V. Filonova (Ministerie van Defensie)	pdf
DMO/DWS&B/AMS/W&ST/BST Defensie Programmabegeleider KLTZ (TD) Ir. M.J. Gram-Blauw	pdf
DMO/Joint IV Commando/C4I&I/ Informatie-Beheer/PDB (Kromhoutkazerne)	pdf
CZSK/MI/MT/SWS/ENGIN Ing. A.S.G. Leus	pdf
CZSK/MI/MT/SWS/ENGIN Ing. A.R. Visser	pdf
CZSK/OPS/NLMF/MWC/R&D Drs. ing. C. Altena	pdf
DMO/DWS&B/AMS/W&ST/IAMD KLTZ (TD) D. Raamsveld	pdf
DMO/DWS&B/AMS/W&ST/IAMD KLTZ H.R.J. Reijenga, MSc	pdf
DMO/DWS&B/AMS/W&ST/BWT KLTZ (TD) Ing. H.M. Verhoeven	pdf
BS/AL/DGB/DOBP/SCIENCE&T KLTZ (TD) Ing. H. T. Lijzenga	pdf
CLSK/PLV C-LSK/DO/C4ISR/SAIR C2 LTKOL F. van Heck	pdf
DMO/DWS&B/DMUNB/LV&M/GLV MAJ Drs. Ing. Huisman	pdf
CLAS/ST CLAS/DIR M&D/AFD MAT/MG A-SYST LTKOL G.N. Marsman	pdf
CLAS/ST CLAS/STAF/AFD S&P MAJ C.T. van der Zeeuw	pdf
BS/AL/DS/Dir. Plan./AfdLuOptr MAJ S.J. Lorraine, BBA	pdf

TNO

Roadmap ISS, S. Ouwejan	email-alert
Programmaleider (PGL) Dr. L. Anitori	email-alert
Research manager PGL Dr. M.B.E.E.S. Deconinck	email-alert
Ir. F.L.M. van den Bogaart	email-alert
Drs. R. van Dijk	email-alert
Dr. Ph. van Dorp	email-alert
Dr. W.L. van Rossum	email-alert
Ir. A. Theil	email-alert
Dr. J.J.M. de Wit	email-alert
TNO Archief locatie Den Haag	link